The Astrophysical Journal, 995:198 (30pp), 2025 December 20 https://doi.org/10.3847/1538-4357/ae14f4

Wind-AE: A Fast, Open-source 1D Photoevaporation Code with Metal and Multifrequency X-Ray Capabilities

Madelyn I. Broome[1], Ruth Murray-Clay[1], John R. McCann[1], and James E. Owen[2,3]
[1] University of California Santa Cruz, 1156 High Street, Santa Cruz, CA 95060, USA; mabroome@ucsc.edu
[2] Imperial Astrophysics, Imperial College London, South Kensington Campus, London SW7 2AZ, UK
[3] Department of Earth, Planetary, and Space Sciences, University of California, Los Angeles, CA 90095, USA
Received 2024 October 9; revised 2025 October 13; accepted 2025 October 16; published 2025 December 16

Abstract

Throughout their lives, short-period exoplanets (<100 days) experience X-ray and extreme-UV (XUV) stellar irradiation that can heat and photoionize planets' upper atmospheres, driving transonic outflows. This photoevaporative mass loss plays a role in both evolution and observed demographics; however, mass-loss rates are not currently directly observable and can only be inferred from models. To that end, we present an open-source fast 1D, XUV multifrequency, multispecies, steady-state, hydrodynamic Parker wind photoevaporation relaxation model based on Murray-Clay et al. The model can move smoothly between high and low flux regimes and accepts custom multifrequency stellar spectra. While the inclusion of high-energy X-rays increases mass-loss rates ($\dot{M}$), metals decrease $\dot{M}$, and the net result for a typical hot Jupiter is a similar $\dot{M}$ but a hotter, faster, and more gradually ionized wind. We find that mulitfrequency photons (e.g., 13.6–2000 eV) are absorbed over a broader range of heights in the atmosphere, resulting in a wind launch radius, $R_{\rm XUV}$, that is of order 10 nanobars for all but the highest surface gravity planets. Grids of H/He solar-metallicity atmospheres reveal that, for typical hot Jupiters like HD 209458b, $R_{\rm XUV} \approx 1.1R_P$–$1.8R_P$ for low fluxes, meaning that the energy-limited mass-loss rate, $\dot{M}_{\rm Elim}(R)$, computed at $R = R_P$ is a good approximation. However, for planets with low escape velocities, like many sub-Neptunes and super-Earths, $R_{\rm XUV}$ can be $\gg R_P$, making it necessary to use $\dot{M}_{\rm Elim}(R = R_{\rm XUV})$ to avoid significantly underestimating mass-loss rates. For both high escape velocities and large incident fluxes, radiative cooling is significant and energy-limited mass loss overestimates $\dot{M}$.

Unified Astronomy Thesaurus concepts: Photoionization (2060); Exoplanet atmospheres (487); Exoplanet atmospheric dynamics (2307); Exoplanet atmospheric evolution (2308); Exoplanet atmospheric structure (2310); Exoplanet atmospheric variability (2020); Exoplanet evolution (491); X-ray astronomy (1810); Hot Jupiters (753); Super Earths (1655); Mini Neptunes (1063); Extreme ultraviolet astronomy (2170)

1. Introduction

Close-in planets are highly irradiated by X-ray (>100 eV) and extreme-UV (EUV, in this paper 13.6–100 eV) photons from their host stars. These high-energy photons can ionize atoms in a planet's upper atmosphere (above the planet's optical transit radius) and heat the layer in the atmosphere where they are absorbed. This heating creates a pressure gradient that drives an outflow known as a Parker wind.

These outflows are observable in transit (for a review, see L. A. Dos Santos et al. 2023), but observational limitations make it difficult to directly map observations to mass-loss rates (E. Schreyer et al. 2024). It is therefore necessary to model atmospheric escape in order to predict mass-loss rates. Constraining mass-loss rates not only allows for the prediction of observables but also is important in tracing the mass-loss histories of exoplanets and understanding their present-day demographics (e.g., E. J. Lee & N. J. Connors 2021; K. Poppenhaeger et al. 2021; J. G. Rogers et al. 2021; D. Kubyshkina & L. Fossati 2022; J. G. Rogers et al. 2024).

However, most currently available models are time-dependent hydrodynamic codes, which are run for many sound-crossing times to reach a steady-state solution, at which point the mass-loss rates can be measured. This approach requires precomputing large grids of mass-loss rates, which can then be interpolated onto evolutionary models (e.g., J. E. Owen & A. P. Jackson 2012; D. I. Kubyshkina & L. Fossati 2021; J. G. Rogers et al. 2021). As model sophistication grows, so does the number of parameters required for any grid, meaning that it is not computationally feasible to use these time-dependent approaches to fully map out the parameter space before they are coupled to any evolutionary calculation. Alternatively, relaxation methods that directly solve for the steady state are much more computationally efficient (R. A. Murray-Clay et al. 2009), so much so that they can be directly coupled to an evolutionary calculation dynamically allowing more parameters to be included and, in principle, more complete physics in the mass-loss model. In this paper, we present a relaxation code with a more complete description of the physics of atmospheric escape than was included in R. A. Murray-Clay et al. (2009).

We take particular care to model the X-ray physics and metal–X-ray interactions, as many exoplanets likely have supersolar atmospheric metallicities (D. P. Thorngren et al. 2016; E. M. R. Kempton et al. 2023; J. Kirk et al. 2025), and the presence of metals in the upper atmosphere can allow X-rays to contribute significantly to the heating and ionizing of the wind (A. García Muñoz 2007). This is the result of two properties of X-rays: (1) X-ray photons are energetic enough that they can induce collisional secondary ionizations via the high-energy photoelectron released when the X-ray photon ionizes a species, and (2) X-ray photons are energetic enough to ionize the K-shell (innermost) electron of certain metals

common to exoplanet atmospheres (e.g., C, N, O, Ne, Mg, Si, and S), giving these metals a larger photoionization cross section at high energies relative to those of the more abundant H and He and allowing X-rays to be absorbed higher in the atmosphere, where they can contribute to driving the wind.

Treating these X-ray properties allows us to model smoothly across the high and low stellar XUV flux regimes without changing any of the assumptions in our model. The outflow is energy limited and is predominantly driven by EUV photons in the low XUV flux limit (e.g., A. García Muñoz 2007; H. Lammer et al. 2014; N. V. Erkaev et al. 2016; J. E. Owen & M. A. Alvarez 2016). In the high XUV flux limit, the contribution of the X-rays is more significant, and the outflow and ionization are balanced by recombination at the base, leading this regime to be referred to as recombination limited (C. Cecchi-Pestellini et al. 2006; J. E. Owen & A. P. Jackson 2012; A. Caldiroli et al. 2022). Since the ratio of the XUV to bolometric luminosity decreases by more than three orders of magnitude over a star's lifetime (e.g., A. P. Jackson et al. 2012; G. W. King & P. J. Wheatley 2021a; L. Affolter et al. 2023) and the ratio of EUV to X-ray luminosity also varies (e.g., J. M. Chadney et al. 2015; G. W. King & P. J. Wheatley 2021a), being able to model smoothly between the high- and low-flux regimes will allow our model to be used to model the evolution of mass-loss rates over Gyr timescales.

While mass loss has been observed around both low (e.g., A. Vidal-Madjar et al. 2003; D. Ehrenreich et al. 2015; M. Zhang et al. 2023) and high (e.g., L. Fossati et al. 2013; A. Lecavelier Des Etangs et al. 2010; B. Edwards et al. 2023) XUV flux stars, observations do not provide model-independent mass-loss rates. For example, for typical systems, Lyα (e.g., A. Vidal-Madjar et al. 2003; D. Ehrenreich et al. 2015) Doppler broadening cannot be used to directly infer mass-loss rates because interstellar medium (ISM) absorption and geocoronal emission obfuscate the Lyα line center, making it impossible to extract the outflow velocity below the sonic point (J. E. Owen 2019). He λ10830 transits (e.g., L. Nortmann et al. 2018; J. J. Spake et al. 2018) are similarly limited by the need for full non-LTE models of metastable helium to back mass-loss rates out of the He λ10830 transits (J. J. Spake et al. 2018; A. Allan & A. A. Vidotto 2019; D. C. Linssen & A. Oklopčić 2023; F. Biassoni et al. 2024). Metal absorption lines may be more direct proxies of the mass-loss rate (e.g., L. Fossati et al. 2013; D. Yan et al. 2022; C. Huang et al. 2023; D. Linssen et al. 2024), but inferring the observability of these lines still requires a model that predicts the velocity and ionization fraction of metals in an outflow (e.g., D. Linssen et al. 2024).

For these reasons, a photoionization-driven atmospheric escape model that includes X-ray physics and metals is a necessary tool for predicting mass-loss rates. A variety of valuable 1D models for photoionization-driven escape exist and are explored in more detail in Appendix A (e.g., R. V. Yelle 2004; F. Tian et al. 2005; A. García Muñoz 2007; J. E. Owen & Y. Wu 2017; I. Malsky & L. A. Rogers 2020; A. Caldiroli et al. 2022; L. A. Dos Santos et al. 2022; T. T. Koskinen et al. 2022; C. Huang et al. 2023; M. Schulik & R. A. Booth 2023; R. Spinelli et al. 2023; D. Kubyshkina et al. 2024). Nevertheless, the ability to quickly forward-model the mass-loss rates and outflow structures of multispecies planetary atmospheres irradiated by both high- and low-flux multifrequency XUV stellar spectra is valuable for parameter studies (this paper; R. O. P. Loyd et al. 2025), predicting observables (A. Pai Asnodkar et al. 2024), and modeling evolution.

To that end, we present `Wind-AE`.[4] `Wind-AE` is a fast, 1D, steady-state forward model for a photoionization-driven transonic Parker wind based on the relaxation model from R. A. Murray-Clay et al. (2009), with XUV multifrequency and multispecies capabilities and self-consistent modeling of the upper atmosphere below the wind.

This open-source code is based in `C` with a Python wrapper that ramps smoothly between solutions that span the range of planetary parameter space (mass, radius, semimajor axis), stellar spectral parameter space (stellar mass and radius, XUV flux, bolometric luminosity, spectrum), and metallicity space (metals, ionization states, and metallicity). The relaxation method reliably finds a solution to two-point boundary value problems but is very sensitive to the proximity of the initial guess to the goal solution in parameter space. The parameter space ramping algorithm allows us to negotiate this sensitivity by stepping strategically through parameter space in order to reach the goal solution. We have the ability to specify metals present, as well as metallicities, but do not include diffusion or drag—an appropriate assumption for metals whose masses are below the crossover mass, which holds for all models in this paper (see M. Schulik & R. A. Booth 2023, for a model with full diffusion capabilities). Nevertheless, `Wind-AE` fills a niche not only with its speed but also with the inclusion of metals and full X-ray ionization physics, as well as the ability to customize stellar spectra and model both the high- and low-flux limit.

In Section 2 we give an overview of the methods we use to model multispecies and multifrequency outflows. We then explore the impact of these additions on the outflow structure and mass-loss rate of HD 209458 b, a Neptune-like planet, and a mini-Neptune in Section 2.4. Finally, in Section 4 we produce high- and low-flux mass-loss grids, and we discuss the parameter space limitations of our model in Section 5.

Additionally, in Appendix A we benchmark `Wind-AE` against existing 1D models for HD 209458 b and GJ 1214 b in the low EUV/XUV flux limit (A. García Muñoz 2007; M. Salz et al. 2016; A. Caldiroli et al. 2022; L. A. Dos Santos et al. 2022; D. Kubyshkina et al. 2024) and for a $1M_J$, $1.7R_J$ planet and WASP-121b in the high XUV flux limit (J. E. Owen & A. P. Jackson 2012; C. Huang et al. 2023).

2. Methods

We have built on the 1D relaxation code presented in R. A. Murray-Clay et al. (2009) by adding multifrequency and multispecies capabilities, as well as updating the way the lower boundary is treated. In Section 2.2 we introduce our model assumptions when solving the mass, momentum, and energy conservation and ionization balance equations (which are given in their generic species- and frequency-independent forms in Section 2.1). Heating and cooling terms are described in Section 2.4. The physical and numerical impacts of adding multifrequency and multispecies capabilities are explored in Section 2.3, along with a more detailed discussion of our spectrum smoothing algorithm (Section 2.3.1) and the X-ray physics (Section 2.3.2), which motivate the multifrequency and multispecies versions of the ionization equation and the photoionization heating rate in the energy equation (Section 2.3.3).

[4] Pronounced "windy." Stands for Wind Atmospheric Escape.

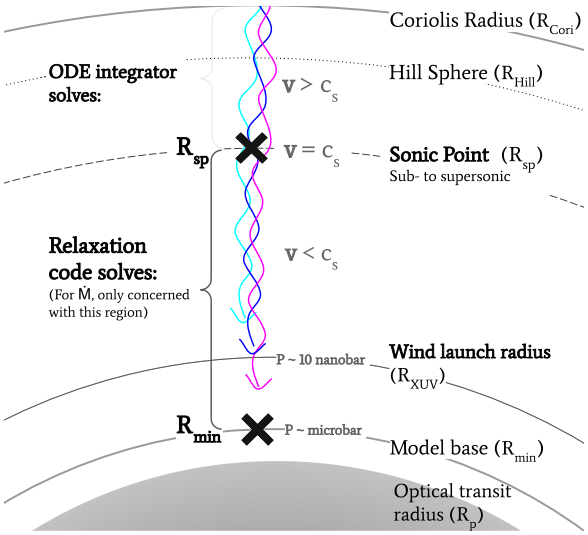

Figure 1. Diagram of wind structure. A thermally driven, Parker-wind-like outflow is driven by photoionization heating, primarily deposited near the wind launch radius ($R(\tau_{XUV}) = 1$). Our relaxation code solves for the structure of this outflow by integrating between two boundary conditions, the minimum radius of the simulation (R_{min}) and the sonic point (R_{sp}), identified by large black crosses. Shorter wavelengths of incident stellar irradiation, like X-rays, are represented by the magenta wave and penetrate deeper into the atmosphere than the longer-wavelength dark purple (higher-energy EUV) and cyan (lower-energy EUV). Magnitude of the local velocity, v, relative to the local sound speed, c_s, is given in the middle column. Important planetary radii in the wind's structure are identified in text in the right column (gray semicircle, R_P; thick solid, R_{min}; thin solid, R_{XUV}; dashed, R_{sp}; dotted, R_{Hill}; thick solid, R_{cori}).

2.1. Species- and Frequency-independent Hydrodynamic Steady-state Parker Wind Equations

We use finite-difference equations and *Numerical Recipes*' relaxation method solver `solvde` (W. H. Press et al. 1992) to solve the substellar 1D spherically symmetric steady-state mass, momentum, energy, and ionization balance equations between upper and lower boundary points (Figure 1). Given the critical point, the "sonic point" (R_{sp}), in the Parker wind transonic solution, the outflow structure becomes a two-point boundary problem, with the upper boundary being R_{sp} and the lower boundary (R_{min}, typically ∼microbar; see Figure 1) being a point lower in the atmosphere than the wind launch radius. We define "wind launch radius" (R_{XUV}, aka photoionization base) to be the lowest radial extent of substantial photoionization energy deposition (see Appendix B for more details). It is, therefore, also the radius where the monoatomic gas starts to accelerate, driven by the pressure gradient generated by ionization heating.[5]

Relaxation is an efficient method for solving two-point boundary value problems (W. H. Press et al. 1992), and it is sufficient to model just the relaxation region, $R_{XUV} < r < R_{sp}$, in order to calculate mass-loss rates. This is because photons absorbed above the sonic point do not contribute significantly to the heating of the atmosphere. The reasons for this are twofold: (1) past the sonic point the wind becomes very optically thin, meaning that it absorbs far fewer photons relative to the optically thicker region below the sonic point, and (2) past the sonic point the flow is supersonic—losing causal contact with the gas below it—and thus the photons absorbed past the sonic point do not contribute to the heating and mass-loss rate of the planet. We do find that computing self-consistent column densities at the sonic point for each atomic species does result in improved mass-loss rate estimates, though, so it is recommended to integrate out to the Coriolis radius in order to compute those values. Unless otherwise specified, `Wind-AE` automatically does so as part of the "polishing" step. Since our model is 1D and flow lines are assumed to be radial, the flow structure is only valid out to the Coriolis turning radius, R_{cori}. We estimate R_{cori} as the radius where the outflow velocity, integrated starting at the sonic point and ignoring pressure acceleration, is deflected by 1 rad owing to the Coriolis force. Past R_{cori}, the velocity of the wind is predominantly set by the gravity of the star and secondarily by interactions with the stellar wind (E. Schreyer et al. 2024). Our method cannot capture any flow and shock structures that result from 3D hydrodynamic effects (J. McCann et al. 2019). In particular, our model will underestimate the density in the region where outflowing gas is shocked by its interaction with the stellar wind. At yet larger radii, the flow is confined into a tube-like geometry often referred to as a "tail" (J. E. Owen et al. 2023; E. Schreyer et al. 2024). Due to this geometric confinement, the density of gas in the tail is larger than computed in our spherically symmetric model. See Appendix B for more details on boundary conditions.

Our 1D slice is placed along the line connecting the substellar point and the star—an approach that has been shown to give good agreement with mass-loss rates from 3D simulations (e.g., J. E. Owen 2020). Along this line, however, tidal gravity and stellar flux have the maximal impact on increasing the mass-loss rate, so extrapolating the mass-loss rate at that location to the rest of the planet's surface would overestimate the total mass loss. Thus, for the results in the main body of this paper, we multiply $\dot{M}$ by a generic reduction factor of 0.3 that encodes adjustments for spherical geometry and horizontal heat redistribution (R. A. Murray-Clay et al. 2009). The equation for surface-averaged mass-loss rate then becomes $\dot{M} = 0.3 \cdot 4\pi R_{sp}^2 \rho(R_{sp}) v(R_{sp})$, in agreement with 3D model results and similar to approaches where the incident flux is divided by 4.

Mass continuity is given by

$$\frac{\partial}{\partial r}(r^2 \rho v) = 0, \tag{1}$$

where the gas density is ρ, gas velocity is v, and distance from the planet's center is r. This equation takes on no species or frequency dependence because we do not model drag, but rather assume a constant mass fraction for each species throughout the wind. Here "species" refers to each unique element, including all of the ionization states of that element. We therefore assume that the species are comoving in the outflow and so share the same velocity. Momentum conservation in a frame rotating with the planet's orbital frequency is

$$\rho v \frac{\partial v}{\partial r} = -\frac{\partial P}{\partial r} - \rho \nabla \phi. \tag{2}$$

For the gravitational potential including stellar tides, ϕ, we use the full form of

$$\phi = -\frac{GM_p}{r} - \frac{GM_*}{r_*} - \frac{1}{2}\Omega^2 r_\perp^2, \tag{3}$$

where, for the substellar point, $r_* = a - r$ and $r_\perp = a\left(\frac{M_*}{M_* + M_p}\right) - r$, where a is the semimajor axis and r is the

[5] Operationally, we compute R_{XUV} as the radial point at which photoionization heating begins to dominate over PdV cooling.

radius from the planet's center. Here G is the gravitational constant, P is the gas pressure ($P = \mu k_B T/\rho$), Ω is the rotation rate of a frame centered on the center of mass of the star–planet system (i.e., the planet's orbital frequency), and M_P and M_* are the planet and stellar mass, respectively. Our tidal gravity term incorporates the transition to Roche lobe overflow, but our code is not designed to model Roche lobe overflow.

In its generic form, energy conservation is

$$\rho v \frac{\partial}{\partial r}\left[\frac{kT}{\mu(\gamma-1)}\right] = \frac{kTv}{\mu}\frac{\partial \rho}{\partial r} + \Gamma + \Lambda. \quad (4)$$

The left-hand side represents the change in the internal thermal energy of the fluid, where k is the Boltzmann constant, $\gamma = 5/3$ for a monatomic ideal gas, and μ is the mean molecular/atomic weight (Equation (14)), which changes self-consistently as a function of radius as the ionization fraction changes. On the right-hand side, the first term tracks PdV cooling (work due to adiabatic expansion of the gas). The heating rate per volume, Γ, is due to radiative heating by bolometric stellar photons absorbed below the wind and to photoionization heating by XUV photons absorbed within the wind. Photoionization calculations now include primary and secondary ionizations and thus gain a dependence on species and frequency (Section 2.3.3). The cooling rate per volume, Λ, now contains not only Lyα cooling, as in R. A. Murray-Clay et al. (2009), but also atomic metal line cooling (Appendix F) inside of the wind and radiative bolometric cooling below the wind. The multispecies and multifrequency versions of these equations and the relevant assumptions are discussed in Section 2.4.

Since much of the energy budget of the wind is set by photoionization, it is also necessary to solve for the ionization balance in the wind, which is, generically,

$$\mathcal{I} = \mathcal{R} - \mathcal{A}. \quad (5)$$

The photoionization rate $\mathcal{I}$ is balanced by the two right-hand terms, which are the radiative recombination rate $\mathcal{R}$ (for which we adopt the uncoupled on-the-spot approximation, meaning that we do not consider the possibility that the resulting photons ionize other species; M. M. Friedrich et al. 2012) and the rate at which ions are advected away, $\mathcal{A}$. R. A. Murray-Clay et al. (2009) showed that collisional ionization is negligible for a pure-H hot Jupiter atmosphere, and we find the same for all planets modeled in this paper. This generic form is expanded into the species- and frequency-dependent form in Section 2.3.3.

Using the species-dependent finite-difference forms of these four equations (Equations (D2)–(D4)), we are able to use the relaxation method to solve for the structure of a hydrodynamic steady-state Parker wind up to the sonic point:

1. total mass density, $\rho(r)$ (see Equation (D1));
2. temperature, $T(r)$ (see Equation (D3));
3. velocity, $v(r)$ (see Equation (D2));
4. per-species neutral fraction, $\Psi_s(r)$ (see Equation (D4));
5. per-species column density, $N_{\mathrm{col},s}(r)$ (see Equation (D5));

We track N_{col} since the neutral fraction is calculated separately for each species. Thus, we need to track the column density of individual species in order to compute the optical depth to photoionizing radiation, τ (M. M. Friedrich et al. 2012).

To navigate the sensitivity of the relaxation method, we have created ramping algorithms that take a series of smaller, adaptive steps in parameter space and reconverge boundary conditions as needed. This allows us to smoothly ramp between solutions that may be too far apart in parameter space to converge to in a single jump.

Our boundary conditions are the temperature, mass density, and per-species neutral fraction at R_{min} and the per-species column density at R_{sp}. While we have the ability to set these BCs explicitly, unless otherwise indicated, in this paper we post facto compute per-species column density self-consistently from the density between the sonic point and Coriolis radius and precompute the lower boundary conditions by assuming that the energy budget between the optical transit radius, R_P, and the wind launch radius, R_{XUV} (where $R_P < R_{\mathrm{min}} < R_{\mathrm{XUV}}$), is dominated by a balance of bolometric heating and cooling and that the temperature structure is isothermal between R_P and R_{min}. These assumptions are only for the purposes of computing more physically informed lower boundary conditions. We do not enforce an isotherm in the region below the wind ($R_{\mathrm{min}} < r < R_{\mathrm{XUV}}$), and we allow the balance between the bolometric heating and cooling, PdV cooling, and other cooling and heating terms to set the temperature structure therein. For detailed derivations of the mass density, temperature, and radius of the base of the simulation, see Appendix B. Note that if the sonic point is outside of the exobase of the planet, the transonic Parker wind solution is not valid and a flag is raised in our model. These planets would not be undergoing mass loss hydrodynamically and would switch to thermal mass loss via Jeans escape. For the purpose of ensuring that all of the outflows in this paper are in the fluid regime, we estimate the exobase using the Knudsen number for hard-body collisions of hydrogen ($\sim 10^{-15}$), which gives a very conservative estimate of the exobase because in an ionized flow the Coulomb cross-section Knudsen number would yield a higher-altitude exobase.

The ionization fraction, velocity, and temperature information at $r > R_{\mathrm{sp}}$ can be of interest when inferring the observability or coupling to other atmospheric escape models, so we also included the ability to integrate the solution outward beyond the sonic point to the Coriolis radius, using *Numerical Recipes*' `odeint` and the Bulirsch–Stoer (`bsstep`) adaptive step-size ordinary differential equation integrator (W. H. Press et al. 1992) with tolerance 10^{-13}.

Integrating outward to the self-consistently computed Coriolis radius, self-consistently converging the column density at the sonic point, and computing the lower boundary density, radius, and temperature, as well as adjusting the molecular-to-atomic-wind transition radius (Section 2.4), constitute the process we call "polishing."

2.2. Model Assumptions

When computing the ionization balance, we include photoionization (including secondary ionization from collisions with photoelectrons), advection, and recombination. Since we are primarily concerned with the wind's launch, we do not model charge exchange, as it has a secondary effect on the net ionization where the wind is launching and requires a more expensive photochemical model (e.g., A. García Muñoz 2007;

C. Huang et al. 2023). We also do not model drag or diffusion, as these require expensive multifluid models (M. Schulik & R. A. Booth 2023). Diffusion of atomic species within the wind should be negligible for species below the crossover mass (D. M. Hunten et al. 1987), as post facto calculations have confirmed that all atomic species in this paper are. If the mass of a species is greater than the crossover mass, its upward diffusion rate is slower than those of the lighter species and it will diffuse throughout the wind and experience drag. Species with masses less than the crossover mass, on the other hand, can be considered entrained in the outflowing gas. This is assumed for all species (neutral and ionized) in the models presented here. Thus, those elements present at the lower boundary of our model (typically 1 μbar) will maintain the same relative abundance throughout the whole upper atmosphere, though their ionization states will change.

When computing heating and cooling, we include photoionization heating, PdV, Lyα, recombination cooling, and, when oxygen and/or carbon species are included in the simulation, O I, O II, O III, C II, and C III line cooling as relevant. These terms represent the first-order heating and cooling sources for the planets in the parameter space we present here. Our model is fully customizable, and other metals and ionization states can be added by users to explore the role of different coolants in the future. We do not model conductive, free–free/bremsstrahlung, or collisional cooling, but we compute them post facto to confirm their irrelevance to the cases we present here. For the puffy planets with low escape velocities and for planets in the high stellar XUV flux limit, conduction and free–free cooling can be a significant energy term; hence, we reserve the implementation of free–free and conductive heating and cooling for future updates of `Wind-AE` and present in this paper only planets for which conduction is not significant (<1% of the energy budget).

2.3. Multifrequency and Multispecies

The photoionization heating rate per unit volume, $\Gamma_{\rm ion}(r)$, and ionization rate per unit volume, $\mathcal{I}(r)$, both contain a dependence on frequency ν and species s in the form of the photoionization cross section $\sigma_s(\nu)$ and number of secondary ionization, $\eta_s(\nu)$. Broadly speaking, the photoionization cross sections, $\sigma_s(\nu)$, for most species, s, are maximal at the species's ionization edge and decrease with increasing energy. Thus, the optical depth $\tau_s(\nu) = N_{{\rm col},s}\sigma_s(\nu) = 1$ surfaces for a species like H I will occur deeper in the atmosphere for higher-frequency photons.

However, the picture is not always so simple. X-rays not only have the ability to ionize more than one species per photon (see Section 2.3.2 for a discussion of secondary ionizations), certain species, such as C, N, O, Ne, Mg, Si, and S, experience a spike in σ_s at high energies (e.g., 120 eV for C). For these species, X-rays above that energy threshold can ionize the innermost, K-shell electron in the atom. The first five of these seven species are predicted to be among the most abundant species in exoplanet atmospheres (e.g., E. M. R. Kempton & H. A. Knutson 2024). Add to this the findings of D. P. Thorngren et al. (2016), which suggest that most exoplanets should have supersolar metallicities, and the interactions between X-rays and metals become essential to accurately modeling where photoionization heating begins to dominate and the wind launches. We reserve a full discussion of metals and high-metallicity physics for a forthcoming paper.

The density and pressure at which the wind launches have a significant impact on mass-loss rates and on the temperature and velocity of the wind, so accurate modeling of the photoionization base is one of the benefits of multifrequency, multispecies modeling.

2.3.1. Multifrequency Spectrum

In order to capture the most important features of a multifrequency spectrum while simultaneously lowering computational cost, we implement multifrequency EUV photons by modeling a smoothed solar spectrum with smoothing bin edges located at the ionization energies of species present in the wind. We employ a custom Savitzky–Golay binning and smoothing algorithm that requires the smoothed spectrum's normalized flux to be equivalent to the flux of the high-resolution spectrum at ionization energies and the relevant K-shell ionization energies of each species included in a simulation (Figure 2). A Savitzky–Golay method is of particular use for fitting polynomials to a spectrum because it locally conserves ionizing energy since the peaks of the spectrum are smoothed and distributed locally. The resultant smoothed spectrum produces identical mass-loss rates and outflow structures (Appendix E, Figure 22). Although the spectrum is dominated by lines, our primary concern in calculating the ionization balance and energetics of the outflow is the integral of the product of the flux and the cross section. Since the cross section varies smoothly with energy, it is acceptable to smooth the spectrum, provided that energy conservation is maintained. See Appendix E for a complete discussion of the smoothing algorithm.

Since XUV stellar spectra are not available for many stars and instrumental observational limitations mean that many "full" stellar spectra are reconstructions, our default spectrum is a flux-scaled version of the `FISM2` (P. C. Chamberlin et al. 2020) solar spectrum, though it is possible to implement unique stellar spectra in our model.

For all of the results presented in this paper we use a scaled solar spectrum. Many atmospheric escape models employ scaled solar spectra to simulate the spectra of stars of a similar type (e.g., A. García Muñoz 2007; M. Salz et al. 2015; T. T. Koskinen et al. 2022; C. Huang et al. 2023; D. Kubyshkina et al. 2024), and it has been shown that the spectral energy distribution (SED) shape affects the upper-atmosphere ionization structure and therefore the outflow structure (J. H. Guo & L. Ben-Jaffel 2016; F. Biassoni et al. 2024; D. Kubyshkina et al. 2024). We find the same when we benchmark against existing 1D models (Appendix A), and the difference can be especially significant for an M dwarf (R. O. P. Loyd et al. 2025) versus solar spectrum, as M dwarfs have higher relative X-ray flux than FGK stars. We reserve an exploration of the impacts of a highly XUV-active star for a forthcoming investigation of HD 189733b, but we do explore the high XUV flux recombination limit modeled by J. E. Owen & A. P. Jackson (2012) in Appendix A.

For the remainder of this paper, when we refer to flux, we will use the following designations: F_* is the total bolometric flux, $F_{\rm tot}$ is a generic total flux over any high-energy spectral range, $F_{\rm XUV}$ is the total flux over 13.6–2000 eV, and $F_{\rm EUV}$ is always the flux in the range 13.6–100 eV, all at the semimajor axis of the planet. These flux values may occasionally be normalized to different energy ranges, and we will identify when we do so. For example, HD 209458's EUV flux is

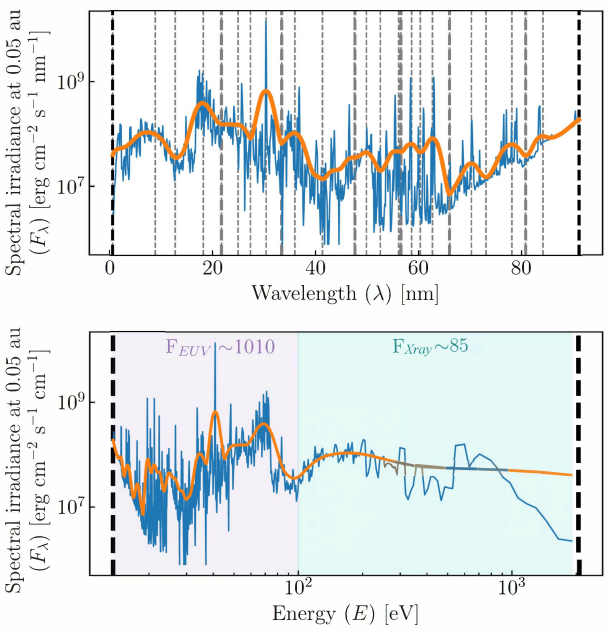

Figure 2. Savitzky–Golay smoothed and binned `FISM2` solar spectrum scaled to 0.05 au—flux at 0.05 au vs. wavelength in nm (top) and vs. energy in eV (bottom). The solid purple and cyan highlights correspond to the EUV (13.6–100 eV) and X-ray (>100 eV) portions of the spectrum, respectively, and the approximate fluxes of each portion are labeled at the top of the bottom panel in erg s^{-1} cm^{-2}. Bin edges (thick vertical dashed lines) are automatically set at ionization edges for species present in a given simulation for maximum accuracy in calculating ionization rates (here pure H). Thin vertical dashed lines are the critical points in the smoothing (Appendix E). We crop our spectra in this investigation at 2000 eV because contributions from higher energies are negligible and most photons of energies >2000 eV have $\tau_\nu = 1$ surfaces below the base of the wind and do not contribute to driving the wind. The XUV smoothed spectrum for a pure-H planetary atmosphere (above) results in 59 wavelength bins, and the EUV one results in 66.

typically quoted in the literature as 450 erg s^{-1} cm^{-2}, which is the total flux over 13.6–40 eV (e.g., A. García Muñoz 2007; R. A. Murray-Clay et al. 2009; T. T. Koskinen et al. 2013; M. Salz et al. 2015). We use this value to normalize our scaled solar spectrum, which makes $F_{\rm EUV} = 1010$ erg s^{-1} cm^{-2} and $F_{\rm XUV} = 1095$ erg s^{-1} cm^{-2}.

2.3.2. X-Rays and Secondary Ionizations

In the case of a star with low XUV flux (typical of an older star), X-rays penetrate deeply into the atmosphere and are absorbed at τ(X-ray) = 1. The τ(X-ray) = 1 surface is typically at pressures $>10^{-9}$ bars, a region that R. V. Yelle (2004), A. García Muñoz (2007), and C. Huang et al. (2023) indicate is dominated by molecules. When low-flux X-rays fall in this region, the majority of the energy the X-rays deposit is radiated away by molecular line cooling (R. V. Yelle 2004; A. García Muñoz 2007, e.g.,). In that case, the wind is instead launched at τ(EUV) = 1, which is higher in the potential well and at a lower density. These "low-flux" winds, therefore, tend to be predominantly EUV driven.

In the case of a star with high XUV flux, the heat deposited by X-rays at τ(X-ray) = 1 is significant enough to contribute to the dissociation of those molecules into atoms. These atoms cannot cool as efficiently as molecules, and as a result, the heat deposited by X-rays is no longer radiated away. Thus, the τ(X-ray) = 1 layer—which is deeper in the potential well than the τ(EUV) = 1 surface and also denser—is able to reach the temperatures necessary to launch a wind. The result is a denser wind and a higher mass-loss rate. Thus, because young stars (<100 Myr old) are expected to have such high relative flux of ionizing XUV photons (e.g., J. M. Chadney et al. 2015; G. W. King & P. J. Wheatley 2020), X-rays are expected to be major contributors to the period of most photoevaporative significant mass loss for planets (e.g., J. E. Owen & A. P. Jackson 2012; C. Cecchi-Pestellini et al. 2006; D. Kubyshkina & L. Fossati 2022).

Properly modeling X-ray physics requires addressing the unique ionization properties of X-rays. First, in the low-flux limit for typical planets, the ionization cross sections, $\sigma(\nu)$, for hydrogen and helium peak at their ionization energies (13.6 and 24.59 eV, respectively) and drop off with frequency. Thus, for a H–He atmosphere, the $\tau(\nu) = 1$ surface where the X-rays are absorbed is too deep in the atmosphere to contribute to heating and driving the wind. This follows from the definition of τ, where $\tau(\nu) = \int_\infty^r (\sum_s n_{0,s}\sigma_s(\nu))dl$ and $n_{s,0}$ is the number density of the lowest ionization state of species, s, where s need not be a neutral atom in the case of our simulation. However, the decrease in $\sigma(\nu)$ with frequency is nonmonotonic for some metals (C, N, O, Mg, Si, and S), giving them an outsized impact on the optical depth at high frequencies despite their much lower relative abundance (Appendix Figure 19).

These species' innermost K-shell electron can be ionized by X-ray photons with energies as low as 124 eV (I. M. Band et al. 1990; Appendix Figure 19), resulting in these metals having comparable EUV cross sections to H and He but much larger X-ray ionization cross sections. Several of those six species are among the most abundant species predicted in exoplanet atmospheres, and even in the relatively small abundances of a 1× solar metallicity atmosphere (M. Asplund et al. 2009; A. B. T. Penzlin et al. 2024) the K-shell ionization cross section of metals weighted by abundance can be an order of magnitude higher than the abundance-weighted hydrogen ionization cross section. It is possible, then, that we may be missing the heating/ionizing contribution of X-rays to planetary outflows—even in the low-flux limit—if we do not take into account metal opacities (e.g., C. Cecchi-Pestellini et al. 2006; A. Caldiroli et al. 2022).

Further complicating the X-ray picture, as seen in A. Gillet et al. (2023), highly energetic X-rays have the ability to ionize more than one atom/ion, which changes the energy and ionization budget throughout the wind depending on the local fraction of the gas that is already ionized (e.g., H. J. Habing & D. W. Goldsmith 1971; J. M. Shull & M. E. van Steenberg 1985; A. Dalgarno et al. 1999). On the whole, when X-rays are absorbed in the atomic upper atmosphere, they are a significant source of flux that may be able to contribute to higher mass-loss rates.

At the same time, metals contribute to higher mean atomic weights, which, when coupled with metal line cooling, may result in lower mass-loss rates than a pure-H model. This effect has been seen in disk photoevaporation models (B. Ercolano & C. J. Clarke 2010) and some atmospheric escape models (C. Huang et al. 2023; D. Linssen et al. 2024). Since X-rays and metals are predicted to have opposite effects, it becomes necessary to model the two together to understand the net effect of including both metals and X-rays on mass-loss rate.

Carefully tracing the distribution of the energy of incident photons is important for capturing the contributions of X-rays

and metals. First, we must determine what fraction, $\epsilon_{s,\nu}$, of the incident photons at each frequency, ν, is absorbed directly by each species, s. We refer to the photon energy minus the energy of the initial ionization as $E_{0,s}$. Then, for X-ray and high-energy EUV photons, we must determine what fraction of the energy, $E_{0,s}$, carried by the photoelectron released during the initial ionization of species s will contribute to heating the gas ($f_{\rm heat}$), what fraction ($f_{\rm ion,tot}$) will contribute to collisionally ionizing other species in the wind, and what fraction will collisionally excite H and be released as Lyα radiation ($f_{\rm excite}$; J. M. Shull & M. E. van Steenberg 1985).

Starting with the fraction of the incident stellar XUV flux at frequency, ν, that is initially absorbed by a species s, then, $\epsilon_{s,\nu} = n_{0,s}\sigma_{s,\nu}/\sum_s n_{0,s}\sigma_{s,\nu}$, where the ν subscript indicates a dependence on frequency, $n_{{\rm col},s}$ is the volumetric number density of a given species, and $\sigma_{s,\nu}$ is the species' photoionization cross section (D. E. Osterbrock & G. J. Ferland 2006). This relation is valid in both optically thin and optically thick regimes (D. E. Osterbrock & G. J. Ferland 2006). Note that the X-ray photoionization cross sections for certain species (C, N, O, Mg, Si, S) are an order of magnitude larger than the species' EUV ionization cross sections because, for those species, even soft X-rays are able to ionize the K-shell electron. In those cases, the electron is removed from the innermost shell rather than the outermost one, and the ionizing energy required to do so is on order of hundreds of eV. K-shell X-ray photoionization cross sections are accounted for using the analytic approximations from I. M. Band et al. (1990). Other photoionization cross sections are computed from the D. A. Verner & G. J. Ferland (1996) database's coefficients and analytic fits.

X-rays further complicate ionization physics by allowing for secondary ionizations by energetic photoelectrons. While it is sufficient to assume that EUV photons are able to ionize only one species, more energetic X-ray photons can carry keV of energy. For example, in the case of a 200 eV X-ray photon ionizing H I, the primary photoelectron released during that initial ionization of H I will have energy $E_{0,\rm HI} = 200\text{–}13.6\,{\rm eV} = 186.4\,{\rm eV}$. Hence, the primary photoelectron has enough energy to ionize several more species in the atmosphere. Thus, each X-ray photon can yield one primary and multiple secondary ionizations.

The number of secondary ionizations, η, that a species s experiences is parameterized using the prescription for a H-dominated atmosphere from J. M. Shull & M. E. van Steenberg (1985), with updated coefficients from A. Dalgarno et al. (1999). We opt for this parameterization rather than a constant η and heating efficiency because where the photoelectron energy is distributed—whether into secondary ionizations or into heat—is a function the local ionization fraction, $\chi(r)$ (J. M. Shull & M. E. van Steenberg 1985; A. Gillet et al. 2023) and therefore will have significant impact on the wind structure. We take $\chi(r)$ to be the total ionization fraction ($\sum_s n_{{\rm ion},s}(r)/\sum_s n_s(r)$) instead of the hydrogen ionization fraction quoted in J. M. Shull & M. E. van Steenberg (1985; $n_{\rm HII}(r)/n_{\rm H}(r)$) and find the difference to be negligible even in high-metallicity cases (though cases where H is no longer the dominant species will require further investigation). This approach is also taken by J. H. Guo & L. Ben-Jaffel (2016). While more sophisticated prescriptions for the distribution of primary photoelectron energy exist (e.g., C. Cecchi-Pestellini et al. 2006; M. Salz et al. 2015), these require radiative transfer calculations or call on CLOUDY (G. J. Ferland et al. 2017), adding computational expense. We compare our wind structure using the J. M. Shull & M. E. van Steenberg (1985) and A. Dalgarno et al. (1999) prescription with the results of radiative-transfer-based escape models in Appendix A.

If the local background ionization fraction, $\chi(r)$, is high—meaning that the most abundant species is largely ionized—a larger fraction, $f_{\rm heat}(r)$, of E_0 will go into heating the gas and a smaller fraction, $f_{\rm ion}$, will go into ionizing the gas. This distribution of energy is the result of elastic collisions between the photoelectrons and the high number of thermal electrons. These collisions transfer most of E_0 to the thermal electrons, resulting in the heating of the gas. The opposite relation holds true if χ is low: the energetic photoelectron is more likely to encounter a neutral atom, $f_{\rm ion}$ is higher, and $f_{\rm heat}$ is lower.

The empirical equations of J. M. Shull & M. E. van Steenberg (1985) for $f_{\rm ion}$ and $f_{\rm heat}$ as a function of χ are good approximations for X-ray stellar photons with energies $>$100 eV. The effect on the wind structure of lowering that energy floor to, e.g., 40 eV is minimal. Above 40 eV, we model secondary ionizations. Below 40 eV, we do not model secondary ionizations and instead assume that E_0 goes entirely into heating.

2.3.3. Species-dependent Versions of Ionization and Heating Equations

Given the effect of secondary ionizations and heating when multiple species are present, we use a species-dependent version of Equation (5) for each species s:

$$\mathcal{I}_s(r) = \mathcal{R}_s(r) - \mathcal{A}_s(r) \tag{6}$$

$$= n_{{\rm ion},s}(r) n_e(r) \alpha_{{\rm rec},s}(r) + \frac{1}{r^2}\frac{\partial}{\partial r}(r^2 n_{{\rm ion},s} v), \tag{7}$$

where $n_{{\rm ion},s}$ and n_e are the number densities of the higher ionization state of species s and *total* electron number densities, respectively. We take $n_e = \sum_s (n_{{\rm ion},s}\zeta_s + n_{0,s}(\zeta_s - 1))$, where ζ_s is the ionization number or the number of electrons removed from species s. The total number density is $n_{{\rm tot},s} = n_{0,s} + n_{{\rm ion},s}$, where $n_{0,s}$ is the number density of the lowest state of species s.

The advection term, $r^{-2}\partial(r^2 n_{{\rm ion},s} v)/\partial r$, in Equation (7) for convenience can be written as $-n_{{\rm tot},s} v \frac{\partial \Psi_s}{\partial r}$ by continuity, where $\Psi_s = n_{0,s}/n_{{\rm tot},s}$ is the number fraction of species s in the lowest state (aka the "neutral" fraction). This is the form we adopt in `Wind-AE`. The recombination coefficient, $\alpha_{{\rm rec},s}$, is temperature dependent and calculated using the recombination coefficient algorithm from CLOUDY (G. J. Ferland et al. 2017).

We define s as the species that is ionized either directly by a stellar photon or secondarily when a stellar photon of energy E_ν first ionizes species j and that ionization releases a primary photoelectron carrying energy $E_{0,j} = E_\nu - {\rm I}_j$, a portion of which goes into collisionally ionizing species s. Our updated local ionization rate per unit volume equation for species s irradiated by an SED with the frequency range $[\nu_{\rm min}, \nu_{\rm max}]$ becomes

$$\mathcal{I}_s(r) \equiv \sum_{\nu=\nu_{\rm min}}^{\nu_{\rm max}} (\mathcal{I}_{1,s,\nu}(r) + \mathcal{I}_{2,s,\nu}(r)), \tag{8}$$

where $\mathcal{I}_{1,s,\nu}$ is the primary ionization rate per unit volume as a function of radius and $\mathcal{I}_{2,s,\nu}$ is the secondary, with

$$\mathcal{I}_{1,s,\nu}(r) = \epsilon_{s,\nu}(r)\Phi_\nu e^{-\tau_\nu(r)}\sigma_{s,\nu}n_{0,s}(r) \quad (9)$$

$$\mathcal{I}_{2,s,\nu}(r) = \sum_{j=1}^{N_{\text{species}}} \mathcal{I}_{1,j,\nu}(r)\eta_{s,j,\nu}(r). \quad (10)$$

The photon flux per spectrum frequency bin is Φ_ν (in units of $\text{cm}^{-2}\,\text{s}^{-1}$), τ_ν is the total optical depth for all species, and $\sigma_{s,\nu}$ is the ionization cross section as a function of frequency and species.

The number of secondary ionizations that species s experiences when impacted by a photoelectron emitted from species j is

$$\eta_{s,j,\nu} = \frac{E_{0,j}f_{\text{ion},s}(r, E_{0,j})}{I_s}, \quad (11)$$

where I_s is the ionization energy of species s. The fractional distribution of photoelectron energy $E_{0,j} = E_\nu - I_j$ when $E_{0,j} > 40\,\text{eV}$ into heat, hydrogen excitations, and secondary ionizations is given by

$$f_{\text{heat}}(r) = 0.9971[1 - (1 - \mathcal{X}(r)^{0.2663})^{1.3163}]$$
$$f_{\text{excite,H}}(r) = 0.4766(1 - \chi(r)^{0.2735})^{1.5221}$$
$$f_{\text{ion,s}}(r, E_{0,j}) = (1 - f_{\text{heat}} - f_{\text{excite,H}})\frac{n_{0,s}\sigma_{\text{col},s}(E_{0,j})}{\sum_m [n_{0,m}\sigma_{\text{col},m}(E_{0,j})]},$$

respectively, where σ_{col} is the collisional ionization cross section (K. P. Dere 2007). This is equivalent to $f_{\text{ion,s}} = n_{0,s}R_s(E_{0,j})/\sum_m[n_{0,m}R_m(E_{0,j})]$, so, for numerical speed, we use the spline tables for R_s, the secondary ionization rate coefficients, from K. P. Dere (2007). The above equation follows from the primary photoelectron energy fraction given by J. M. Shull & M. E. van Steenberg (1985) and ionization rate coefficients given by K. P. Dere (2007). This form allows us to easily add secondary ionizations to our ionization rates by tracing the number of secondary ionizations each photoelectron released produces. Recall that when $E_{0,j} < 40\,\text{eV}$, $f_{\text{heat}} = 1$ and $f_{\text{ion,s}}$ and $f_{\text{excite,H}}$ are 0.

The photoionization heating term for the energy conservation equation (Equation (4)) then becomes

$$\Gamma_{\text{ion}}(r) = \sum_s \sum_{\nu=\nu_{\min}}^{\nu_{\max}} \mathcal{F}_{s,\nu}(r)e^{-\tau_\nu(r)}\sigma_{s,\nu}n_{0,s}(r), \quad (12)$$

where $\mathcal{F}_{s,\nu}(r)$ is the energy flux of photoelectrons that goes into heating the gas and

$$\mathcal{F}_{s,\nu}(r) = (E_\nu - I_s)[\epsilon_{s,\nu}(r)\Phi_\nu]f_{\text{heat}}(r). \quad (13)$$

Excited H releases an Lyα photon that we assume escapes, resulting in radiative cooling. We find that for HD 209458 b for a H–He atmosphere these excitations account for a total of 14% of the total incident energy (Figure 3). Monte Carlo radiative transfer calculations confirm that a little more than half of Lyα photons generated by H excitations owing to collisions with nonthermal electrons escape upward to space and more than 99% leave the simulation domain through either the upper or lower boundary without being thermalized (see Appendix C). We expect Lyα photons that exit through the lower boundary to be effectively lost and not to contribute to heating the outflow. Nevertheless, we conduct a sensitivity test by modeling HD 209458 b with 0% of nonthermally excited Lyα photons escaping and 100% converted into heat. We find that the effect on the mass-loss rate and structure of the planet is negligible.

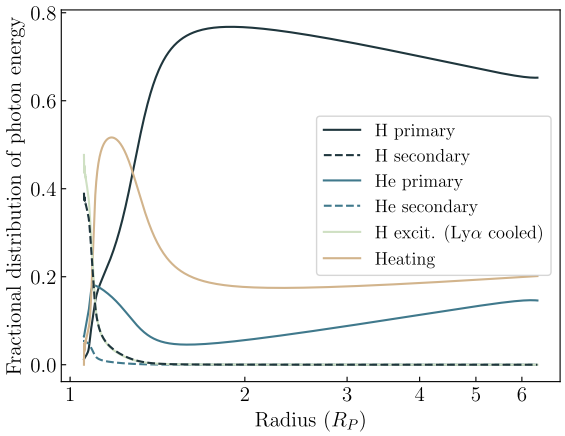

Figure 3. Energy deposition fraction for HD 209458 b—fraction of total incident stellar energy into ionizing hydrogen (black), helium (navy), heating (tan), and hydrogen excitation (light green) of which, in our model, 100% is assumed to escape as Lyα radiation. Total XUV flux over 13.6–2000 eV is 1095 erg s^{-1} cm^{-2}.

The J. M. Shull & M. E. van Steenberg (1985) approximation for the secondary ionization rate of metals is not expected to be appropriate for high metallicities (>50Z), and future iterations of this model will include appropriate high-metallicity physics. However, for low metallicities, we are able to model any species for which photoionization cross sections and collisional ionization rate coefficients as a function of frequency are available.

2.4. Heating and Cooling Terms

Below the photoionization base, the atmosphere is molecular and the temperature structure can often be approximated by an isotherm at the skin temperature (T. Guillot 2010). Often, this region is treated as having a constant isothermal base temperature inferred from equilibrium temperature models (which is an oversimplification; V. Parmentier & T. Guillot 2014; V. Parmentier et al. 2015) or estimates for similar planets, and this temperature is used as a lower boundary condition at some radius higher than R_P. More sophisticated and expensive models (e.g., C. Huang et al. 2023) perform full lower-atmosphere photochemistry calculations to obtain more physical and accurate temperature and density structure, and we compare to such models in Appendix A.

We elect for an approximation somewhere between the two approaches. We directly compute the skin temperature (Equation (B4)) as the balance between bolometric heating and cooling and use the assumption of an isotherm and a constant mean molecular weight to compute the microbar radius as our simulation base given a measured optical transit radius (see Appendix B). Because we do not treat molecules or photochemistry in our model, we set a constant mean molecular weight,[6] $\mu_{\text{mol}}(r)$, for all points below the wind and force μ to transition to the numerically solved mean atomic

[6] For the results shown in this work $\mu_{\text{mol}} = 2.3m_{\text{H}}$, which is the mean molecular weight of H_2 and He in solar abundances.

weight, $\mu(r)$. We do so smoothly, by multiplying $\mu_{\rm mol}$ by a complementary error function normalized to 1 (Equation (B6)) that drops off as the wind becomes optically thin (Appendix Figure 20), the molecules photodissociate, and ionization heating begins to dominate, launching the wind. As a result, we can write $\mu(r)$ in units of g for all r in the simulation as

$$\mu(r) = \mu_{\rm mol}(r)\,{\rm erfc}'(x) + \mu_{\rm atom}(r)[1 - {\rm erfc}'(x)] \quad (14)$$

$$= 2.3 m_{\rm H}\,{\rm erfc}'(x) + \frac{m_{\rm H}\cdot[1 - {\rm erfc}'(x)]}{\sum_s Z_s \frac{m_{\rm H}}{m_s}(2 - \Psi_s(r))}, \quad (15)$$

where the mean molecular weight of the species explicitly modeled in our outflow, $\mu_{\rm atom}(r)$, includes electrons, ions, and neutral atoms and hence changes as a function of radius as the gas ionization state evolves. As we currently do not model multiple ionization states per atom, we can simplify the traditional definition of $\mu_{\rm atom}(r)$ to be in terms of Ψ_s, the "neutral" fraction (fraction of the species in the lowest ionization state). Here $m_{\rm H}$ is the atomic mass of hydrogen, m_s is the atomic mass of species s in the wind, and Z_s is the mass fraction of that species. The complementary error function is discussed in more detail in Appendix B.

We use the same error function to force the optical ($\kappa_{\rm opt} = 0.004$) and IR opacities ($\kappa_{\rm IR} = 0.01$; T. Guillot 2010) in the bolometric heating (Equation (19)) and cooling equations (Equation (18)) to drop off at the same transition point as the molecular-to-atomic transition (Appendix B). The result is that the bolometric heating and cooling that dominated below the wind give way to photoionization heating and atomic line cooling within the wind. This simplification does not affect hot Jupiters but will likely be important for puffy sub-Neptunes (Section 5.1). Future work explicitly modeling the physics in this region is merited (for more on the impacts of lower-atmosphere modeling, see Appendix Figures 15 and 18).

Above the photoionization base (~10 nanobars), the wind is generally atomic and the energy budget (Equation (4)) is set by a balance of photoionization heating, advective heating, cooling due to *PdV* work (gas expansion), recombination cooling, Lyα cooling, and metal line cooling. For the planets in this paper, as modeled in other approaches (e.g., D. Kubyshkina et al. 2018b; A. Caldiroli et al. 2022; T. T. Koskinen et al. 2022; C. Huang et al. 2023; D. Linssen et al. 2024), it is reasonable to assume that this is optically thin line cooling, but other regions of parameter space where this may not be an appropriate assumption merit further investigation. In addition, most likely, H_{3+} cooling (R. V. Yelle 2004; A. García Muñoz 2007) and other molecules (T. Yoshida et al. 2022, 2024) also play a significant role in cooling in the molecular region below the wind, absorbing and radiating away the highest-energy photons of the XUV irradiation.

The cooling term, however, is now $\Lambda(r) = \Lambda_{\rm Ly\alpha}(r) + \Lambda_{\rm metal}(r) + \Lambda_{\rm bolo}(r)$, with

$$\Lambda_{\rm Ly\alpha}(r) = -7.5\times10^{-19} n_e n_{\rm HI} e^{-11834K/T}, \quad (16)$$

where n_e is the number density of total electrons, $n_{\rm HI}$ is the number density of neutral H, T is temperature in kelvin, and all vary as a function of radius. $\Lambda_{\rm Ly\alpha}$ is radiative cooling from the Lyα line of atomic hydrogen, $\Lambda_{\rm metal}$ is radiative cooling from metal lines, and $\Lambda_{\rm bolo}$ is bolometric cooling from thermal emission in the molecular layer of the atmosphere, where we assume that radiative cooling can be treated with an average infrared opacity (T. Guillot 2010) rather than needing to be modeled line by line. All cooling rates are per unit volume and have units of erg s^{-1} cm^{-3}. In Appendix C we verify that most of the Lyα photons escape the wind into space and the vast majority leave the domain of our simulation through either the upper or lower boundary before being thermalized, verifying that thermal Lyα cooling is well treated by Equation (16).

In the atomic outflow, when O II, O III, C II, and/or C III are present in the simulation, we have found the corresponding lines to be nonnegligible coolants at high fluxes, and D. Linssen et al. (2024) find Fe II and Ca II line cooling to be significant in high-metallicity cases (which are not treated in this paper, and thus these lines are neglected for the time being). There is some debate as to whether Mg is a net heater or coolant (L. Fossati et al. 2013; C. Huang et al. 2017), so here we choose to initially work with O and C, and our model can handle further line coolants to explore their role in the future. Line cooling is generally most impactful at high fluxes. However, even at low fluxes, some Lyα photons are able to escape the outflow and cool the wind, making it the second most significant contribution to the cooling of the wind after *PdV* cooling.

A fully complete description of metal line cooling would require additionally tracking the energy levels of each metal ion. Such an approach would likely require at least tens of more fields per atom/ion, which would quickly become computationally infeasible. However, the spontaneous decay timescales of most energy levels that produce strong cooling in the optical/UV are extremely short, with only some metastable levels (e.g., O I/O III $1D_2$) approaching a few hundred seconds (e.g., W. L. Wiese et al. 1996). These decay timescales are typically much shorter than the flow timescale; therefore, we can approximate that the level populations in an individual atom/ion are in *local* collisional statistical equilibrium. Furthermore, given that the temperatures we find in our simulations are typically $\lesssim 10^4$ K, we can make the nebular approximation (e.g., D. E. Osterbrock & G. J. Ferland 2006) and ignore excitations from excited permitted levels, along with recombinations to excited states for determining the level populations. This allows us to simplify the level populations of each ion/atom and model metal line cooling using a two-level atom model, where, following M. Schulik & J. E. Owen (2025b),

$$\Lambda_{\rm metal}(r) = -\sum_s n_e n_{{\rm ion},s}\left[A_s \frac{\exp\left(-\frac{T_{{\rm line},s}}{k_b T}\right)}{n_e\left(1 + \frac{n_{c,s}}{n_e}\right)}\right], \quad (17)$$

where $n_{\rm ion,s}$ is the number density of O II, O III, C II, and/or C III and the constants A_s, $T_{{\rm line},s}$, and $n_{c,s}$ are derived from G. J. Ferland et al. (2017) and `CHIANTI` (K. P. Dere et al. 1997; G. Del Zanna et al. 2015). These constants are derived by fitting this two-level atom model to the cooling rates numerically calculated using the `CHIANTI` database in the temperature range 500–20,000 K. In the `CHIANTI` calculations we include all the energy levels and transitions; however, we still assume a statistical collisional equilibrium *within* each atom/ion.[7] We find that this approach accurately models the true cooling function to within an accuracy of a few percent.

[7] We note that while `CHIANTI` is a collisional plasma code, since our outflow is photoionization and advection dominated, we only use `CHIANTI` to compute the level populations of individual atoms/ions in a collisional statistical equilibrium and switch off collisional ionization terms, as appropriate within the framework of the nebular approximation.

The values of the species-dependent constants A_s, $T_{\mathrm{line},s}$, and $n_{c,s}$ are listed in Appendix F, along with comparisons of our two-level model to the fully numerically computed cooling rate. We note that these are exactly the same approximations and approach as those made by previous work to determine Equation (16) to model Lyα cooling.

The final cooling term is the bolometric cooling, which is discussed in more detail in Appendix B:

$$\Lambda_{\mathrm{bolo}}(r) = 2\sigma_{\mathrm{SB}} T_{\mathrm{skin}}^4 \rho(r) \kappa_{\mathrm{IR}} \,\mathrm{erfc}'(x). \tag{18}$$

Here σ_{SB} is the Stefan–Boltzmann constant; T_{skin} is the skin temperature, which we take to be $T(R_{\mathrm{min}})$; and κ_{IR} is the IR opacity. In the atomic/ionized wind, line cooling dominates; however, in the molecular region between R_{min} and R_{XUV}, where it is optically thick to most XUV photons and, in the low-flux limit, the highest energy X-ray photons are radiated away by molecular line cooling, our assumption that bolometric cooling dominates provides a reasonable approximation. If the photodissociation front extends beyond the wind launch radius and molecules survive into the wind, transitioning at R_{XUV} as we do in this paper would no longer be appropriate. We explore the limits of these assumptions in the low escape velocity limit in Section 5.2, but for the majority of planets in this investigation we can safely assume that the molecules have photodissociated and/or thermally dissociated below R_{XUV}. To approximate this behavior, we multiply κ_{IR} and κ_{opt} (the optical opacity) by the same complementary error function (Equation (B6)) as is used in Equation (14), which lowers these opacities to zero so that the bolometric cooling does not unphysically dominate in the atomic wind. This transition is visible at $\sim 1.1 R_P$ in Figure 5.

The same is done for the bolometric heating term,

$$\Gamma_{\mathrm{bolo}}(r) = F_* \rho(r) \left(\kappa_{\mathrm{opt}} \mathrm{erfc}'(x) + \frac{1}{4} \kappa_{\mathrm{IR}} \mathrm{erfc}'(x) \right), \tag{19}$$

where F_* is the single-band bolometric flux, which is an independent variable that is not dependent on the chosen SED shape or integrated XUV flux (F_{tot}). In this double-gray approximation, the total heating then becomes $\Gamma(r) = \Gamma_{\mathrm{ion}}(r) + \Gamma_{\mathrm{bolo}}(r)$.[8] The photoionization heating term that dominates in the wind, Γ_{ion}, is also now species dependent and also incorporates the contribution to heating by highly energetic primary photoelectrons released during the ionization of each initial species by a high-energy X-ray photon (Equation (12)). The species- and frequency-dependent Γ_{ion} equation is discussed in detail in Section 2.3.

3. Results of Introducing Multifrequency and Multispecies Assumptions

3.1. Multispecies and Multifrequency

Though metals are required to understand the true impact of X-rays on an outflow, for clarity we first consider the difference between a wind launched by a multifrequency spectrum and one launched by a monofrequency spectrum in a low-to-moderate-flux pure-H atmosphere, illustrated in Figure 4. In the following section, we build up incrementally from the results presented in R. A. Murray-Clay et al. (2009) to elucidate the individual contributions of multifrequency X-rays, metals, and boundary conditions. There has, naturally, been more detailed work since R. A. Murray-Clay et al. (2009), and we compare to those models in Appendix A and Section 5.4.

If we first implement multifrequency X-rays without metals, as expected, the effect of adding X-ray photons (cyan), compared to a spectrum that extends only to the EUV (purple), is negligible since metals are not present in the atmosphere (Figure 4). In addition to exploring the impact of mono- versus multifrequency stellar spectra, Figure 4 also highlights the impact of our lower boundary condition assumptions.

The differences in density, temperature, and ionization fraction structure between the two monofrequency models stem from differences in the structure of the bolometrically heated region below the wind, which sets the radius at which the ionizing photons that drive the wind are deposited. R. A. Murray-Clay et al. (2009) do not treat this region and do not include either the molecular or bolometric correction and simply solve for that region assuming the same physics as the rest of the wind. Our updated boundary conditions yield a somewhat puffier atmosphere below the wind. We refer to this as increased "bolometric puffing," a process that is also modeled analytically and discussed in J. E. Owen & H. E. Schlichting (2023). Absorption of the 20 eV photons occurs at approximately the same pressure and density in both models; however, increased bolometric puffing increases the radius at which that density and pressure occur. This launches a wind from higher in the planet's potential well, where less work needs to be done to reach the planet's escape velocity. As a result, the velocity of the outflow is higher (Figure 4, gray vs. black dashed–dotted lines).

R. A. Murray-Clay et al. (2009) found that the wind structure and mass-loss rate are relatively insensitive to changes in the temperature at the base of the simulation ($T(R_{\mathrm{min}})$); this remains true. In general, anything that results in a wind being launched from shallower within the potential well, such as the bolometric puffing, will result in a faster, hotter outflow with a higher $\dot{M}$ (Figure 4).

The wind launch radius, R_{XUV}, is often cited as 1 nanobar pressure (e.g., R. A. Murray-Clay et al. 2009). With the inclusion of multifrequency XUV irradiation and a solar-like spectrum, however, we find that the winds for most planets launch closer to 10 nanobars, irrespective of planet mass. This is a result of the higher-energy photons in a multifrequency spectrum being deposited at a lower radius where the density is $\sim 10\times$ higher than the radius at which monofrequency 20 eV photons are absorbed.

In other words, solutions for hot Jupiters with moderate escape velocities and ionizing fluxes like the one in Figure 4 are not very sensitive to including a pseudomolecular region below the wind with a higher mean molecular weight and bolometric heating and cooling (Section 2). However, inclusion of this layer can change the lower boundary dramatically for planets with lower escape velocities at the planet's radius, R_P, including many sub-Neptunes (J. E. Owen & H. E. Schlichting 2023). This agrees with the findings of, e.g., A. Allan & A. A. Vidotto (2019), who found that mass-loss rates were sensitive to surface gravitational potential.

[8] Full derivation in Appendix B.

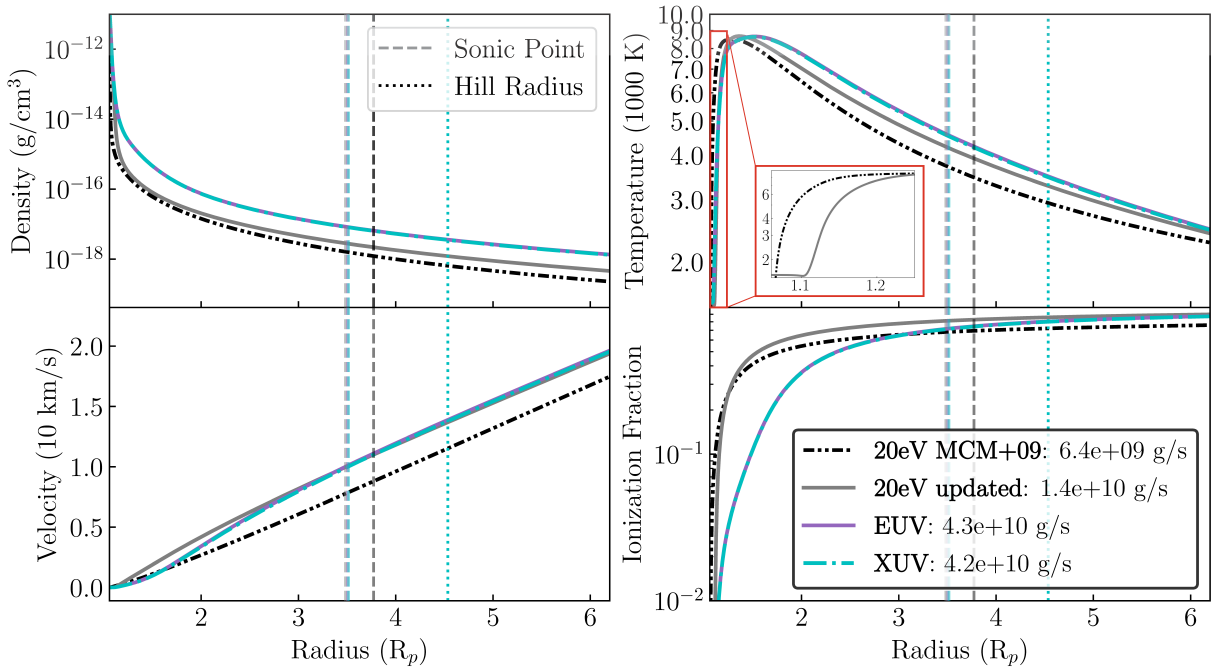

Figure 4. Multifrequency profiles for a pure-H HD 209458 b. The black dashed–dotted line is the original 20 eV monofrequency and pure-H R. A. Murray-Clay et al. (2009) model ($R_{\rm min} = 1.037 \quad R_P$, $\rho(R_{\rm min}) = 2.7 \times 10^{-11}$ g cm, $T(R_{\rm min}) = 1000$ K). The gray solid line is also monofrequency 20 eV, but with our updated physical lower BC and bolometric heating and cooling at the base ($R_{\rm min} = 1.057\ R_P$, $\rho(R_{\rm min}) = 1.8 \times 10^{-11}$ g cm^{-3}, $T(R_{\rm min}) = 1534$ K). The remaining plots all use the updated BCs. Purple is the EUV multifrequency (13.6–100 eV) version. Because no metals are present, X-rays (cyan, dashed–dotted, XUV 13.6–2000 eV) contribute relatively little to the profiles or mass-loss rates of a pure-H atmosphere, so the solutions overlie the EUV. Stellar spectra in all simulations are normalized to 450 erg s^{-1} cm^{-2} between 13.6 and 40 eV (in keeping with R. A. Murray-Clay et al. 2009). Our model is not valid past the Coriolis radius (upper limit of x-axis). The sonic point and Hill sphere are given by dashed and dotted lines, respectively.

While hot Jupiters typically have wind launch radii $R_{\rm XUV} \sim 1.1R_P$–$1.3R_P$, planets with lower escape velocities may have $R_{\rm XUV} \gtrsim 2R_P$–$8R_P$. Many works model mass loss using the energy-limited mass-loss rate $\dot{M}_{\rm Elim} = \varepsilon F_{\rm XUV}\pi R^3/GM_P$, where ε is the efficiency, M_P is the planet's mass, and R is chosen to be R_P, the IR photosphere radius (e.g., N. V. Erkaev et al. 2007; D. Kubyshkina et al. 2018a). Therefore, for low escape velocity planets, the energy-limited mass-loss rate evaluated with R_P equal to the planet's optical transit radius can dramatically underestimate the mass-loss rate (Figure 10). This finding is consistent with the literature (e.g., N. V. Erkaev et al. 2016; D. Kubyshkina & L. Fossati 2022; C. Huang et al. 2023); we discuss the outflow behavior in the high and low escape velocity limits in more detail in Section 5.

The remainder of the solutions in Figure 4 all use the physical lower BCs detailed in Appendix B. The frequency-dependent forms of Equations (8) and (12) allow us to trace the distribution of the photon energy throughout the wind. Here we choose to scale a `FISM2` (daily average from 2009 January 1; P. C. Chamberlin et al. 2020) solar XUV SED to $F_{\rm XUV} = 1095\,{\rm erg\,s^{-1}\,cm^{-2}}$ (normalized such that the integrated flux between 13.6 and 40 eV is $450\,{\rm erg\,s^{-1}\,cm^{-2}}$), which is the flux of HD 209458, a late F-type or early G-type star, experienced by planet b.

Changing the energy distribution of incident photons from a single frequency to multiple frequencies has the most significant impacts on the density and ionization structure of the wind (Figure 4). To see why this is the case, consider the energy between 13.6 and 20 eV in the scaled solar spectrum. The 13.6–20 eV photons represent 40% of the total flux in the spectrum. Placing these photons all at 20 eV overestimates the resulting heating and underestimates the ionization fraction. Notice that, relative to the monofrequency solution, the EUV solution in Figure 4 has a higher mass-loss rate by a factor of 3 and an equal wind velocity.

The total flux, $F_{\rm tot}$, of stellar photons is normalized in both the EUV and XUV cases such that the flux of photons with energies in the EUV range 13.6–40 eV is equivalent to the flux at 20 eV in the monofrequency case. This means that simulations quoted as XUV (spanning 13.6–2000 eV) have a higher $F_{\rm tot}$ than those quoted as EUV (spanning 13.6–100 eV, unless otherwise noted[9]). The changes in temperature profile between the monofrequency results in Figure 4 in gray and the multifrequency results in cyan and purple can be attributed in equal part to the presence of multifrequency photons and higher $F_{\rm tot}$.

Figure 5 shows the source of these multifrequency-induced structural changes in the wind. When compared to a monofrequency 20 eV solution with the same lower boundary physics and conditions, the energy of a 20 eV photon is absorbed much higher in the atmosphere. This phenomenon is the result of the higher-energy photons penetrating deeper into the atmosphere, puffing it up, raising the scale height of the atmosphere and causing lower-energy photons to be absorbed higher in the atmosphere. Thus, the flux of a multifrequency spectrum is deposited over a much broader physical range of $\tau(\nu) = 1$ surfaces. This can explain the broadened peak in both

[9] Existing mass-loss rates and outflow profiles in the literature frequently quote the integrated EUV flux as the flux between 13.6 and 40 eV (see Appendix A), so when comparing to those solutions we normalize our $F_{\rm tot}$ such that the integrated flux between 13.6 and 40 eV matches the quoted values.

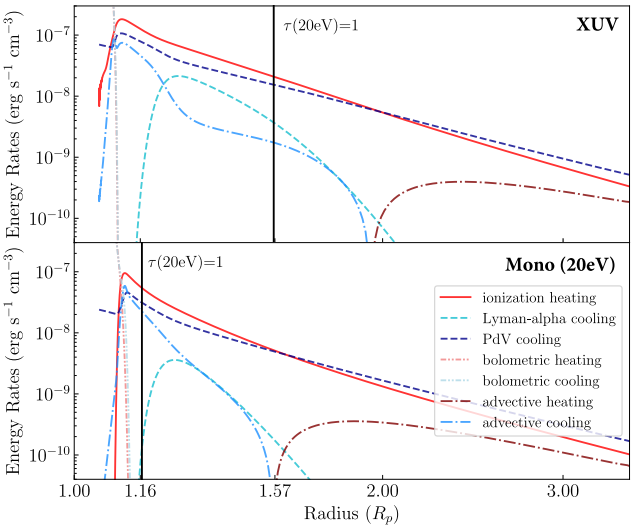

Figure 5. Energy plot for pure-H XUV versus monofrequency HD 209458 b—energy structure of multifrequency XUV solution (top panel, cyan solution in Figure 4) and 20 eV monofrequency solution (bottom panel, gray solution in Figure 4). The $\tau(20\text{ eV}) = 1$ surface for the XUV multispecies is at a higher radius because the deeper penetration of high-energy XUV photons puffs up the atmosphere, resulting in higher densities and optical depths at higher radii than in the monofrequency solution.

the energy deposition (Figure 5) and the temperature (Figure 4) with radius.

The addition of metals somewhat tightens this radius range of XUV energy deposition (Figure 6) and shifts it deeper into the potential well. When we add both X-rays and metals in solar abundance ($Z_\odot$) to the planet HD 209458 b (Figure 6), we see that the higher-ionization cross sections of metals mean that some of the X-rays are absorbed in the atomic layer and contribute to the wind, rather than being deposited deep below it. Our spectral range is lowered to 11.26–2000 eV to capture the first ionization energy of C I, and we do not lower to the ionization energy of Mg I (7.65 eV), as Mg I is immediately ionized to Mg II, whose ionization energy is 15.04 eV. Thus, the integrated flux is 1185 erg s^{-1} cm^{-2}. Although we reserve a full exploration of the effect of metallicity for a future investigation, even in solar abundances the metals have a significant role to play in the structure of the wind (if less so in the mass-loss rate for moderately irradiated hot Jupiters). The mass-loss rate is similar for both the single-species and multispecies planets because, taken independently, the metals and X-rays have opposite effects on $\dot{M}$.

The metals increase the mean atomic weight, lowering the scale height and increasing the density and opacity of the outflow (Figure 6), but, more importantly, lowering the sound speed, c_s, which raises the sonic point of the outflow (an isothermal Parker wind has its sonic point at $R_{\rm sp} = GM_p/(2c_s^2)$). Therefore, multiple species lower the mass-loss rate owing to their effect on μ. Conversely, X-ray photons penetrate deeper into the atmosphere than EUV photons do. Because the density is higher at these greater depths, X-rays can drive an outflow that is more massive, slower, and more ionized thanks to secondary ionizations.

3.2. Tidal Gravity and Comparison to Energy Limit

Returning to the canonical example of HD 209458 b—this time with a H–He atmosphere—we also plot $\dot{M}$ as a function of semimajor axes spanning from 0.03 to 0.7 au. A changing semimajor axis, a, not only influences the amount of flux at the planet's location but also affects the stellar tidal gravity (Equation (3)). We plot a high ($L_{\rm XUV}/L_{\rm tot} = 10^{-4}$) and low XUV luminosity ($L_{\rm XUV}/L_{\rm tot} = 10^{-6}$) series to approximate the behavior of young and old stars, respectively (Section 3.3). It is intentional that we do not include lower fluxes for the "old star" lower flux case, because while those stellar fluxes corresponding to $a > 0.4$ au can launch winds, conductive cooling becomes significant at those extremely low fluxes. We do not model conductive cooling, so we exclude all simulations for which post facto calculations of the conductive cooling rate per unit volume as a function of radius show it to be $\geqslant$5% of the total heating rate per unit volume.

Since $F_{\rm tot} \propto a^{-2}$ and the tidal gravity term is $\propto a^{-3}$, the tidal gravity is significant for close-in planets but negligible at larger semimajor axes. The transition is illustrated by the lower-flux old star in Figure 7. Along with our model's $\dot{M}$, we plot the energy-limited $\dot{M}_{\rm Elim}(\varepsilon) = \varepsilon F_{\rm tot}\pi R_P^3/GM_P$, where ε is the efficiency with which stellar photon energy is converted to heat, and the tidally corrected energy-limited

$$\dot{M}_{\rm tidal}(R,\,\varepsilon) = \frac{\varepsilon F_{\rm tot}\,\pi R^3}{GM_P}\left(1 - \frac{3}{2\xi} - \frac{1}{2\xi^3}\right)^{-1}, \qquad (20)$$

where $\xi = R_{\rm Hill}/R_P$, the ratio of the planet's Hill sphere and R, where R is traditionally taken to be R_P (N. V. Erkaev et al. 2007).

The energy-limited mass-loss approximation is an upper limit on a planet's mass-loss rate that assumes that the incident stellar flux is converted with efficiency, ε, into heating the wind and driving an outflow. Planets with lower incident stellar flux are generally said to be in the "energy-limited" regime, meaning that the mass-loss rate is directly proportional to flux and adding additional flux will result in a higher $\dot{M}$—to a point. Once a planet has sufficiently high flux, the limiting factor on $\dot{M}$ is the rate at which species can recombine and the planet is said to have entered the "recombination-limited" mass-loss regime. We directly compute ε for each point in this plot by computing the frequency-averaged efficiency of energy deposition into heat (as opposed to ionizations), taking into account secondary ionizations. Radiative cooling is not included in our efficiency. We find that our values range between $\varepsilon \sim 0.3$ and 0.4.

For the "old" star with the present-day $L_{\rm XUV}$ of HD 209458, $\dot{M}$ approaches the tidally corrected energy limit for very close-in planets but diverges for planets at larger separations (Figure 7(a); M. Schulik & J. Owen 2025a). Despite having flux two orders of magnitude higher, the "young" star does not approach the energy limit, because the Lyα cooling is more significant for higher-flux stars because the planets' upper atmospheres are able to reach temperatures closer to the $\sim$10,000 K at which Lyα cooling efficiency peaks.

The dependence of $\dot{M}$ on tidal gravity also results in an update to Figure 7 of R. A. Murray-Clay et al. (2009), which plotted $\dot{M}$ as only a function of changing $F_{20\text{ eV}}$ (which was the total flux concentrated at 20 eV). With the inclusion of XUV multifrequency radiation and a H–He atmosphere with $F_{\rm tot}$ normalized such that the flux in the EUV range of 13.6–40 eV is the same as the $F_{20\text{ eV}}$ in R. A. Murray-Clay et al. (2009), if the planet's distance is held constant at 0.05 au, we reproduce a similar result (Figure 7(b)). The characteristic relationship found by R. A. Murray-Clay et al. (2009), where $\dot{M} \propto F_{20\text{eV}}^{0.9}$ in

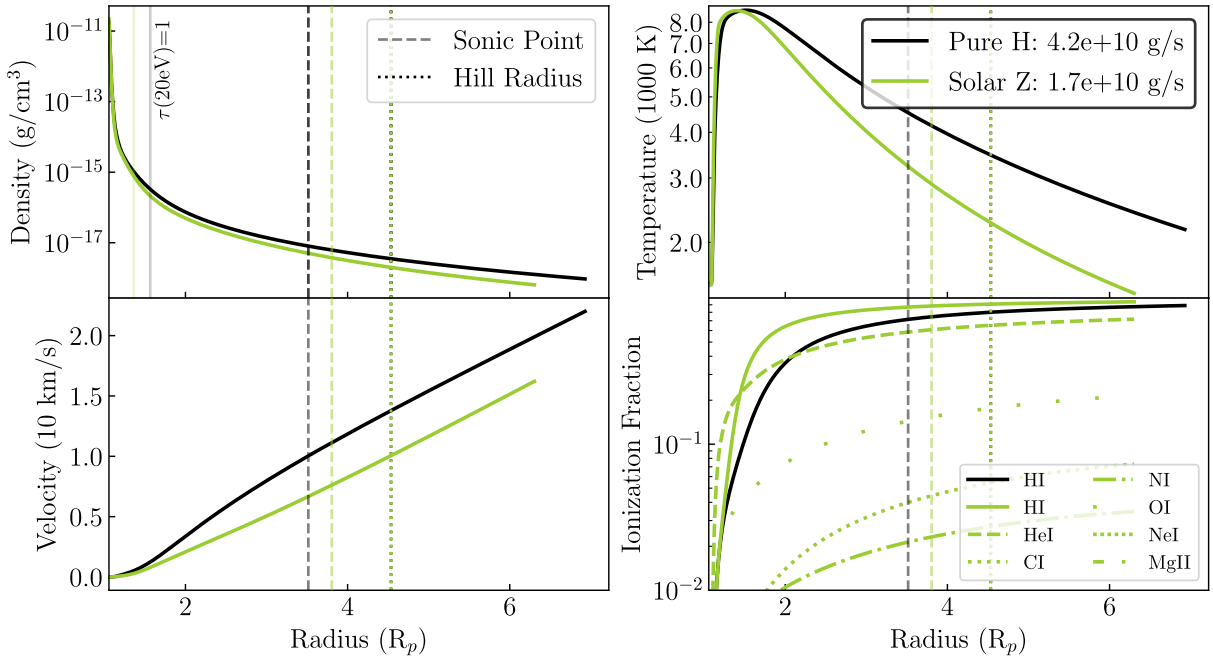

Figure 6. HD 209458 b multispecies—pure hydrogen (black) and solar abundances of H I, He I, C I, N I, O I, Ne I, and Mg II (green) XUV (11.26–2000 eV) solutions. Vertical lines: sonic points (dashed), Hill radius (dotted), $\tau(20\,\mathrm{eV}) = 1$ surfaces (light solid); solutions end at the Coriolis radius for each simulation.

the energy-limited regime (low fluxes) and $\dot{M} \propto F_{20\mathrm{eV}}^{0.6}$ in the recombination-limited regime (high fluxes), holds when distance is held constant. Tidal gravity is present in both models, but its impact is not noticeable without changing the semimajor axis. When the semimajor axis is also changed, the magnitude and slope of the flux–$\dot{M}$ relationship change significantly as a result of tidal gravity. Our derived lower boundary temperature, $T(R_{\mathrm{min}})$, also has a semimajor axis dependence (Appendix B), but tidal gravity is the dominant contributor to the mass-loss rate.

The aiding effect of tidal gravity is evident where the orange and cyan lines intersect with the gray line in Figure 7(b). At 0.05 au, the tidal gravity is equivalent to the case in which distance is held constant. At 0.03 au, the tidal gravity contribution elevates the mass-loss rate above that of the equivalent flux at 0.05 au. We can turn off tidal gravity in our simulations, but we elect to keep it on, as it has a significant effect on mass-loss rates for planets whose potential well would otherwise be too deep to launch a wind.

3.3. As a Function of Planet Type

The additions of multifrequency photons and multiple species highlighted the importance of where in the potential well the wind launches. Planet mass and radius, then, are unsurprisingly important since the planet's escape velocity sets the amount of energy required to lift the wind out of the potential well.

For an approximately 5 Gyr old solar-mass and solar-luminosity star, we model three generic planets of varying sizes located at 0.05 au. The first is a hot Jupiter of $0.7M_{\mathrm{J}}$ and $1.4R_{\mathrm{J}}$, the second is a Neptune-mass and Neptune-radius planet, and the third is a super-Earth with 5 $M_{\oplus}$ and 2 $R_{\oplus}$ (Figure 8).

We compute the total XUV flux (13.6–2000 eV) from the stellar age–XUV flux relation in G. W. King & P. J. Wheatley (2021a). For a 4.5 Gyr old star like our Sun, the ratio of XUV to total bolometric luminosity has been estimated to be $L_{\mathrm{XUV}}/L_{\mathrm{bol}} \sim 10^{-6}$. We take it to be $F_{\mathrm{tot}} = 1095\,\mathrm{erg\,s^{-1}\,cm^{-2}}$, appropriate for the low-activity Sun. These models, as well as all others henceforth, model a H–He atmosphere where the mass fraction in H is 0.8 and that in He is 0.2. The escape velocity at R_P of the hot Jupiter is the highest of the three planets ($v_{\mathrm{esc}} = 4.6 \times 10^6\,\mathrm{cm\,s^{-1}}$). The Neptune-like planet has $v_{\mathrm{esc}} = 2.4 \times 10^6\,\mathrm{cm\,s^{-1}}$, and the super-Earth has $v_{\mathrm{esc}} = 1.8 \times 10^6\,\mathrm{cm\,s^{-1}}$.

For the hot Jupiter, the scale height is smaller and photons are absorbed closer to the planet's surface (optical transit radius) than on smaller planets, resulting in a wind that launches from a relatively lower R_{XUV} (Figure 8). This radius is deeper in the potential well, so the wind requires more heating in order to escape the planet's gravitational pull, so the outflow has a much higher maximum temperature of 8800 K than the Neptune-like planet (3600 K) and the super-Earth (2900 K). One consequence of this much higher temperature is that the Lyα cooling is more significant for the hot Jupiter, which, along with the rapid drop in density with radius, results in the steep drop-off in temperature. The small scale height means that the hot Jupiter also absorbs the incident multi-frequency photons over a smaller range of heights in the atmosphere, which gives the much narrower temperature peak and the faster ionization with radius. The rapid ionization with radius is also a result of the distribution of stellar photon and photoelectron energy between heating and ionization.

A hotter wind is almost always a faster wind, and the three planets are consistent with this relationship. Because the smaller planets absorb photons over a broader range of radii, require less heating to launch a wind, and thus have a slower decrease in density with radius, they also ionize more slowly as a function of planetary radius. For all planets, at the lowest radii in the wind, the ionization fraction of He is higher than that of H. This is particularly pronounced for the super-Earth.

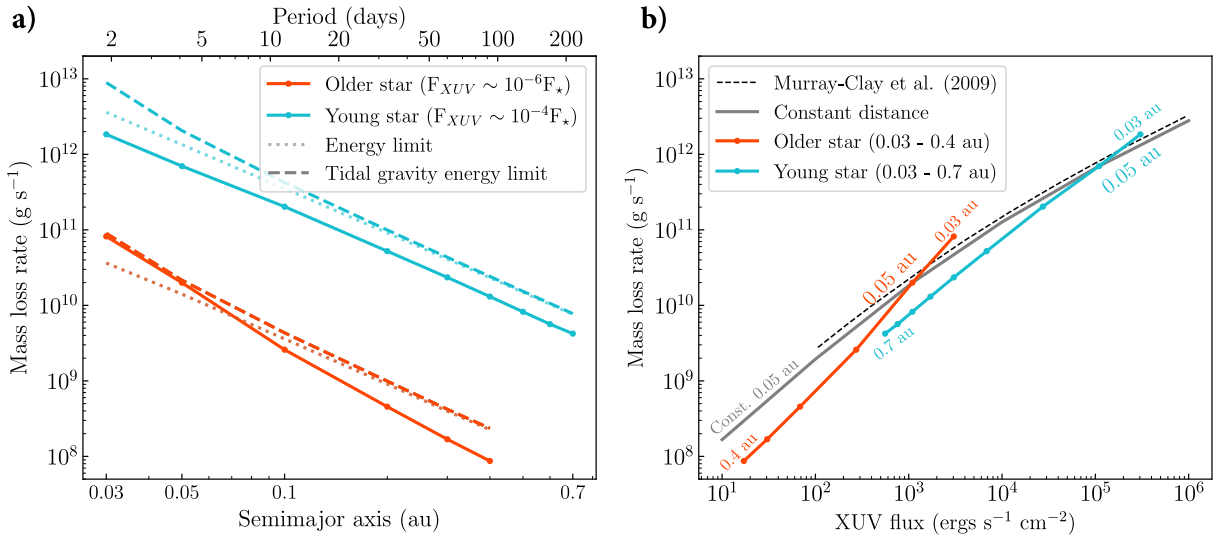

Figure 7. $\dot{M}$ and tidal gravity. (a) $\dot{M}$ for a planet with parameters of HD 209458 b and a multifrequency XUV, H–He atmosphere is plotted as a function of semimajor axis, a, in au (solid lines) for a high XUV activity, "young" HD 209458 ($L_{\rm XUV} \sim 10^{-4}L_*$; cyan) and lower XUV flux, older HD 209458 ($L_{\rm XUV} \sim 10^{-6}$ L_*; orange). Lower/moderate flux is $F_{\rm XUV} = 1095$ erg s^{-1} cm^{-2} and high flux is $F_{\rm XUV} = 1.095 \times 10^5$ erg s^{-1} cm^{-2} at 0.05 au, and the stellar spectral shape does not change. Flux scales with a^{-2}. Traditional energy-limited $\dot{M}$ (dotted) and the N. V. Erkaev et al. (2007) tidal-gravity-corrected energy limit $\dot{M}$ (dashed) with our modeled efficiencies (average 0.37, computed point by point as described in Section 3.2) are plotted for both flux regimes. (b) Mass loss is plotted as a function of XUV flux. We reproduce Figure 7 of R. A. Murray-Clay et al. (2009; black dashed) for a pure-H, 20 eV monofrequency simulation, in which semimajor axis is held constant while flux at 0.05 au is varied. The $\dot{M}$ values are multiplied by the geometric reduction factor of 0.33 for consistency with our current results. The gray line is an update of the previous constant distance line, now with an XUV multifrequency spectrum and a H–He atmosphere. The computed $\dot{M}$ values for young and older stars from the left are overplotted. The difference in slope is the result of tidal gravity. We assume that all planets are tidally locked, meaning that we use a constant geometric reduction factor.

4. Mass-loss Grids for H–He Atmospheres

4.1. $\dot{M}$ as a Function of Planetary Parameters

Since the relaxation method is relatively fast, we are able to run a grid of 663 points inexpensively.[10] The majority of the time per grid point is the "polishing" process in which we enforce self-consistency in the upper and lower boundary conditions. This speed was aided by our choice to create a nonlinear grid that spans the total mass range of $0.009M_{\rm J}$–$1.66M_{\rm J}$ (3–528 $M_\oplus$) and a radius range of $0.165M_{\rm J}$–$2.02R_{\rm J}$ (1.85–22.65 $R_\oplus$). The 53 steps in radius space are linear, but the masses are chosen such that the grid lines constitute lines of constant escape velocity, $M_{P,\rm init}/1.85\ R_\oplus$, where $M_{P,\rm init}$ is the linear array of 12 initial masses that span from 3 to 43 $M_\oplus$. These mass and radius ranges are chosen to cover the range of observed masses and radii of super-Earths, sub-Neptunes, and hot Jupiters with semimajor axes of 0.05 au. The results are presented in Figure 9 for an "old" star flux (left) and a "young" star flux (right).

The grid is limited by a number of numerical and physical limitations. The lower end of the mass range of super-Earths ($M_P \leqslant 3.5\ M_\oplus$) is limited by the numerical failure to converge to a wind solution. Notably, this failure is not purely numerical in nature. These planets are so low in escape velocity and optically thick that $R_{\rm XUV}$ computed using the lower BC scheme in Appendix B can be as large as $8R_P$.

In these extreme cases, when we compute the sonic point for a wind driven purely by bolometric radiation, $R_{\rm sp,bolo} \approx GM_P/(2c_s^2)$ for the sound speed, c_s, at the $R_{\rm min}$, we find that $R_{\rm sp,bolo}$ is of order $R_{\rm XUV}$. This means that the bolometric heating is sufficient to launch a transonic wind and the XUV photons are being absorbed near or within the supersonic region of the wind. The XUV photons cannot contribute to heating and driving a wind; hence, these flows are likely not photoionization-driven winds, but rather are still undergoing boil-off or core-powered mass loss (as in J. G. Rogers et al. 2021; Y. Tang et al. 2024). Therefore, we do not include those solutions in these grids. We also indicate the region for which $R_{\rm sp} \leqslant R_{\rm Hill}$, the Hill sphere, with hatch marks in Figures 9 and 10. Note that these hatches do not represent a strict limit for `Wind-AE`'s applicability (see Section 5.2 for a complete discussion).

The lower escape velocity limits seen in the grids are the result of the bolometric luminosity and XUV flux we have chosen. Because we created a grid based off of the parameters of the quintessential photoevaporating planet, HD 209458 b, a hot Jupiter with $L_* = 1.78\ L_\odot$ at 0.05 au and $F_{\rm tot} = 1095$ erg s^{-1} cm^{-2}, super-Earths and low-mass sub-Neptunes are so highly irradiated proportional to their escape velocities that they are on the verge of core-powered mass loss and potentially Roche lobe overflow. While `Wind-AE` is able to solve for some of these planets (at the left edge of the grids), it struggles to converge beyond that because even our "lower flux" grid has a moderately high bolometric and XUV flux.

We make a similar cut at the upper end of masses. Our maximum initial mass for $R_P = 1.85\ R_\oplus$ is 43 $M_\oplus$ to avoid unphysically dense planets. `Wind-AE` is capable of modeling these extremely dense planets, though at high enough escape velocities it eventually suffers from numerical and physical difficulties discussed in Section 5.1. However, we cut off our grid at the high escape velocity end because, for lower $F_{\rm XUV}$, conductive heating and cooling are significant and we do not model conduction in this paper (grayed-out region in Figures 9 and 10).

[10] About 1 hr run in "embarrassingly parallel" (aka 10 simultaneous sequential runs of ~70 planets each) on an eight-core laptop with an M1 chip. Relative computation time comparisons are made in Appendix A.

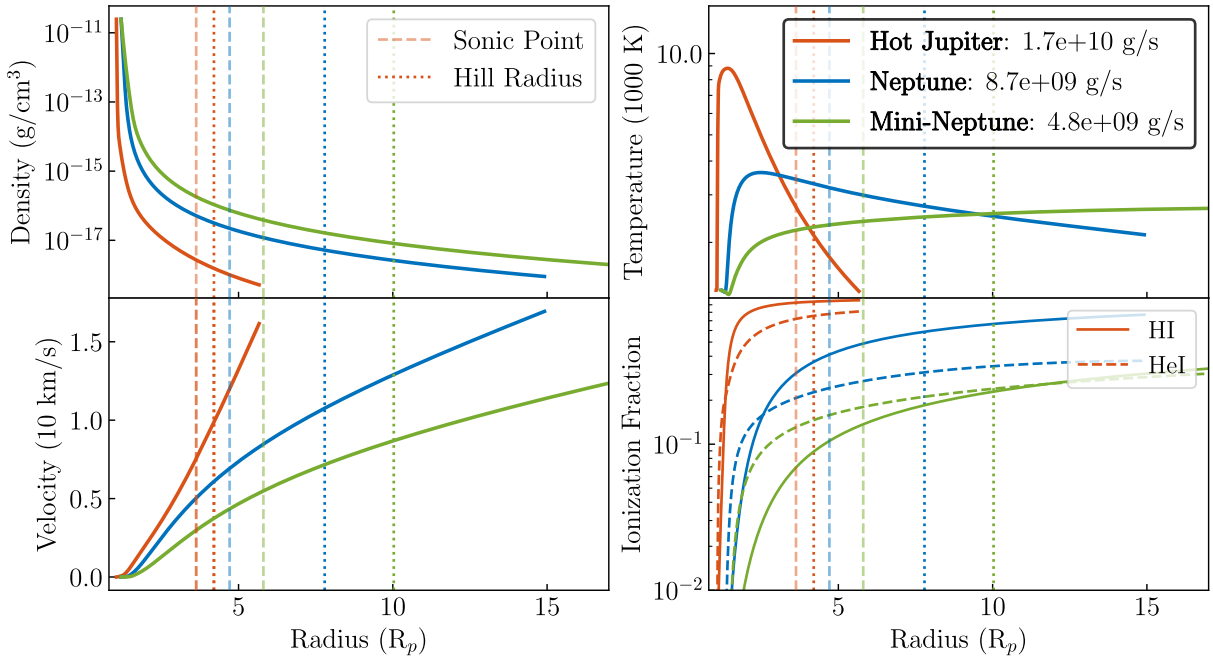

Figure 8. Hot Jupiter, Neptune, and mini-Neptune H–He outflows—wind structure of H–He (0.8:0.2 mass fraction) atmospheres for a $0.7M_J$, $1.4R_J$ (222.6 $M_\oplus$, 15.7 $R_\oplus$) planet (orange) with escape velocity at R_P of $v_{esc} = 4.6 \times 10^6$ cm s^{-1}; a Neptune-sized 17 $M_\oplus$, 3.9 $R_\oplus$ planet (blue) with $v_{esc} = 2.4 \times 10^6$ cm s^{-1}; and a mini-Neptune with 5 $M_\oplus$, 2 $R_\oplus$ (green), and $v_{esc} = 1.77 \times 10^6$ cm s^{-2}. All three are located at 0.05 au around a 1 $M_\odot$ and 1 $L_\odot$ star, with total flux at 0.05 au of $F_{tot} = 1095$ erg s^{-1} cm^{-2} (13.6–2000 eV). All are plotted in terms of their R_P, but all have different R_P values. The super-Earth's small thermal inversion below the wind (where larger planets have an isotherm) is the result of bolometric heating/cooling naturally falling off before photoionization heating becomes significant and the wind launches.

We plot the fractional difference of our computed values of $\dot{M}$ from the energy-limited estimate, $(\dot{M} - \dot{M}_{\rm tidal})/\dot{M}_{\rm tidal}$ in Figure 10, with the heating efficiencies computed point by point as before (for the lower flux case $\langle\varepsilon\rangle = 0.37$, high flux $\langle\varepsilon\rangle = 0.33$). Given that $\dot{M}_{\rm tidal}(R, a, \varepsilon)$ is the theoretical upper limit on mass-loss rates, it should not be possible for our mass-loss rates to be higher for the same efficiency value, ε, as the amount of red in Figure 10(a) seems to suggest. However, $\dot{M}_{\rm tidal}$ is derived assuming that all of the photon energy is deposited near $R_{\rm XUV} \approx R_P$ and that the optical transit radius, R_P, is frequently used in the energy-limited mass-loss equation. This assumption is a good one for hot Jupiters with moderate XUV instellation. However, as we have seen, for planets with lower escape velocity, multifrequency photons and bolometric heating/cooling below the wind drive $R_{\rm XUV} \gg R_P$. Likewise, when we plot the ratio between the tidally corrected energy-limited mass-loss rate, $\dot{M}_{\rm tidal}(R_P, a, \varepsilon)$, and the $\dot{M}$ found by our model (Figure 9, bottom panels), we see that for these high escape velocity planets $\dot{M}$ is more than an order of magnitude below the energy limit. Thus, $\dot{M}_{\rm tidal}(R_P)$ will always underestimate the energy-limited mass-loss rate for lower escape velocity planets and overestimate it for high escape velocities at moderate XUV fluxes. Instead, it is necessary to use $\dot{M}_{\rm tidal}(R_{\rm XUV})$.

Indeed, when we compute $\dot{M}_{\rm tidal}(R = R_{\rm XUV}, 0.05{\rm au}, \varepsilon)$, for the lower flux grid we see that our mass-loss rates are below this photoionization-radius-corrected mass-loss rate (Figure 10(b)) and thus do not violate the maximum energy available. Note that the valley feature in Figure 10(b) can also be seen in Figure 13 of J. E. Owen & A. P. Jackson (2012), though we disagree with some of the aspects of the model therein and provide more detailed comparisons in Appendix A.

The findings in Figure 10 differ slightly from the results of D. Kubyshkina et al. (2018a), who found that the tidally corrected energy-limited mass-loss rate computed at $R_{\rm XUV}$ for a heating efficiency of 0.15 underestimates mass-loss rates for the lowest-density planets. The D. Kubyshkina et al. (2018a) grids span lower planetary radii and masses (1–10 $R_\oplus$, 1–39 $M_\oplus$ vs. our 1.85–22.65 $R_\oplus$, 3.8–528 $M_\oplus$) than our model can currently do without conductive cooling, but the lower left quadrant of, e.g., Figure 10 corresponds to a similar range of masses and radii.

The primary source of the discrepancy is the efficiency in Equation (20). When we compare our mass-loss rates to $\dot{M}_{\rm tidal}(R_{\rm XUV}, \varepsilon = 0.15)$ as in D. Kubyshkina et al. (2018a) instead of the escape-velocity-dependent $\varepsilon = 0.26$–0.38 in Figure 10(b), we likewise find that $\dot{M}_{\rm tidal}$ overestimates the mass-loss rates for low-density planets. It is also likely that we find slightly higher $R_{\rm XUV}$ on average than the $R_{\rm eff}$ computed by D. Kubyshkina et al. (2018a). Both methods take the absorption radius to be the point of maximum ionization, but the input stellar spectrum in D. Kubyshkina et al. (2018a) is parameterized as two monofrequency EUV (20 eV) and X-ray (247 eV) bins. This is an appropriate parameterization for computational efficiency but, as Figure 5 shows for monofrequency EUV versus multifrequency XUV, will result in a slightly lower estimate for $R_{\rm XUV}$.

These discrepancies further validate the ultimate conclusion of D. Kubyshkina et al. (2018a): regardless of the relative accuracy of the energy-limited approximation for lower-flux planets, it still requires accurately estimating both $R_{\rm XUV}$ and the heating efficiency a priori.

For planets in the high-flux limit, however, it is not necessary to find $R_{\rm XUV}$ to compute a reasonable estimate for the tidally corrected energy-limited mass-loss rate. In

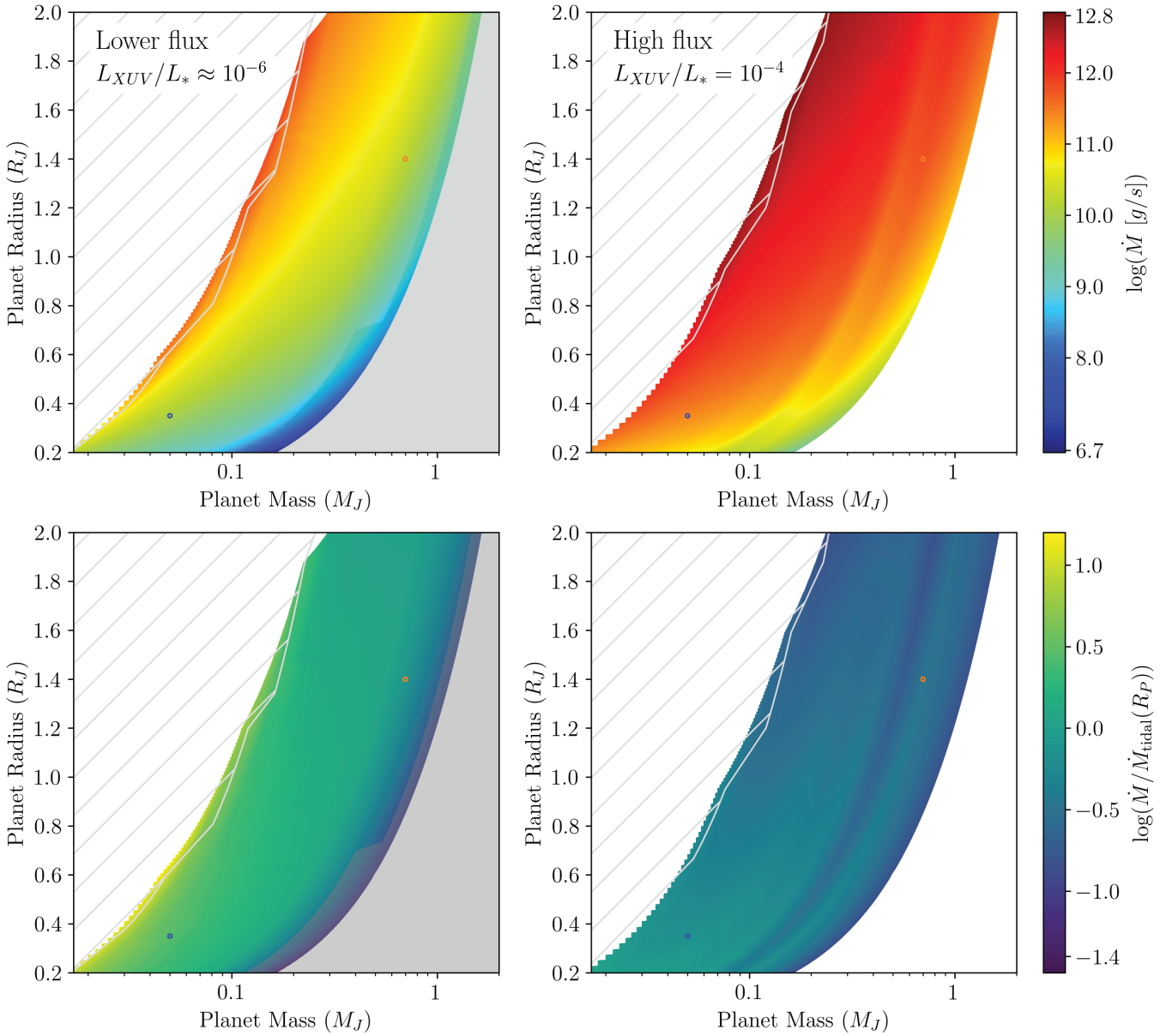

Figure 9. H–He $\dot{M}$ grids for low and high fluxes—2D linearly interpolated grid of 663 H–He planets located at 0.05 au around a solar-mass, solar-luminosity star. Fluxes correspond to an old star ($F_{\rm XUV} \approx 10^{-6} F_*$) of 1095 erg s^{-1} cm^{-2} (left column) and a younger star ($F_{\rm XUV} \approx 10^{-4} F_*$) of 109,500 erg s^{-1} cm^{-2} (right column). Locations of a Neptune analog and an HD 209458 b analog are plotted as blue and orange points, respectively. The grayed-out region represents where conductive cooling—which we do not model—would be significant. The hatched region represents planets for which $R_{\rm sp} \leqslant R_{\rm Hill}$ (see Section 5.2). The top row is color-mapped to the log of the mass-loss rate in g s^{-1}, and the bottom row to the log of the ratio of $\dot{M}$ with the tidally corrected energy-limited $\dot{M}(R_P)$ (Equation (20)) with efficiencies calculated on a point-by-point basis in the grid (low-flux $\langle\varepsilon\rangle \approx 0.37$, high-flux $\langle\varepsilon\rangle \approx 0.33$). See Section 5.1 for a discussion of the bifurcation near $0.1 M_{\rm J}$ in the high-flux grids.

Figure 10 we do not show the fractional difference for the high-flux case, because the planets are in the radiation/recombination-limited mass-loss regime, meaning that radiative cooling is energetically important. As such, $\dot{M} < \dot{M}_{\rm tidal}(R_P)$ for the extent of the high-flux grid.

Slices of an even higher flux grid are included in Appendix A, Figure 17, where we compare to the high XUV flux limit mass-loss rate grids of J. E. Owen & A. P. Jackson (2012). In short, we find that the lack of *PdV* and Lyα cooling in the J. E. Owen & A. P. Jackson (2012) model results in very different mass-loss rates across the grid, highlighting the importance of those two cooling sources even in recombination-limited outflows.

5. Discussion

5.1. High Escape Velocity Limit

Atmospheric escape in the high escape velocity limit ($\gtrsim 5 \times 10^6$ cm s^{-1}) will be explored in more detail in future works, but we make note of a couple of interesting features here. The first few numerical and physical complications result from the small scale height that results from high escape velocity at large planet masses.

A small scale height not only yields an atmosphere that is more compressed; it also means that most of the ionizing photons are absorbed very deep in the potential well. This means that it can be difficult for these planets to launch winds,

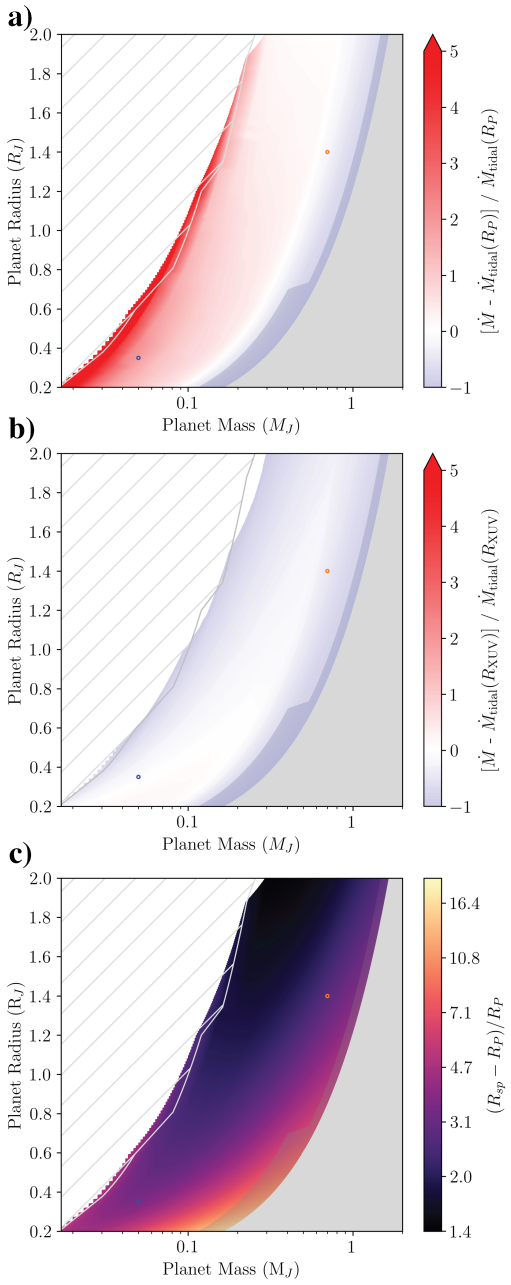

Figure 10. H–He $\dot{M}$ relative to energy-limited mass-loss rates. (a) Lower flux (1095 erg s^{-1} cm^{-2}) fractional difference $(\dot{M} - \dot{M}_{\rm tidal}(R_P))/\dot{M}_{\rm tidal}(R_P)$, from tidally corrected energy-limited mass-loss rate computed at R_P. We use the same grid as in Figure 9. Orange and blue circles correspond to an HD 209458 b analog and Neptune analog, respectively. Red indicates that $\dot{M}_{\rm tidal}$ underestimates the mass-loss rate computed by our model, and blue indicates that $\dot{M}$ is less than the energy limit, as is expected. (b) Same color-bar scaling as in panel (a), but here we plot $(\dot{M} - \dot{M}_{\rm tidal}(R_{\rm XUV}))/\dot{M}_{\rm tidal}(R_{\rm XUV})$à. (c) Height of the sonic point above R_P in units of R_P. All $R_{\rm sp}$ are below the Hill radii, except at the lowest escape velocity edge (off the left edge of the panel), where the outflow transitions to boil-off or core-powered mass loss—evaluation of our code's performance in this regime is beyond the scope of this work.

since they require a large flux to achieve sufficient energy to launch. For the same reason, these outflows can reach >4000 K before launching (e.g., the temperature difference between planets of varying surface gravity in Figure 8). Inspection of these planets' energy distributions reveals that they experience significant Lyα cooling, even when they experience relatively low fluxes. Lyα cooling is significant for these planets because their deep potential wells necessitate high temperatures to escape, so these atmospheres heat to high temperatures where Lyα is efficient before the atmosphere outflows. This agrees with the analytic predictions of J. E. Owen & Y. Wu (2016).

Even when `Wind-AE` can find a solution, for high escape velocity and lower-flux planets, the default base boundary condition radius of the 1 μbar radius may not capture all of the $\tau(\nu) = 1$ surfaces for the highest-energy photons. Instead, the wind launches immediately at the base of the simulation and $R_{\rm XUV} = R_{\rm min}$. In these cases, when computing our grids, we raise $T(R_{\rm min})$ several thousand kelvin from the expected temperature in the bolometrically heated region, $T_{\rm skin}$, to account for the fact that we are essentially beginning our model mid–wind launch (see Appendix B for more details). Because we do not capture all of the photoionizing photons in our simulation, we lose up to 10% of the flux out of the bottom of the simulation. We have validated that this procedure provides a good match for solutions that set the simulation base at higher densities and take substantially longer to converge but do not lose flux out the bottom (Appendix B, Figure 21). Making the adjustment to $T(R_{\rm min})$ results in a similar wind structure (Figure 21)) and brings $\dot{M}$ to within a factor of, on average, 1.5 of the $\dot{M}$ for the simulation whose base is set deeper in the wind.

Despite this, the transition from $R_{\rm XUV} > R_{\rm min}$ to $R_{\rm XUV} < R_{\rm min}$ is likely the source of the sharp transition near $0.1 M_J$ visible in the high-flux grids (Figure 9) and the energy-limited mass-loss rate comparison plots (Figures 10(a) and (b)). This indicates that while this approximation brings $\dot{M}$ close to the expected value, it still systemically underestimates it slightly along the line of constant escape velocity that starts at $0.1 M_J$, though the general trend across the grid still holds. The other consequence of not being able to trace the deposition of the highest few energies of photons is that we compute a lower average heating efficiency than expected if all photons were captured. Thus, we include a warning in `Wind-AE` when $R_{\rm XUV} < R_{\rm min}$.

The reasons we opt for this simplification rather than raising the pressure of the base boundary for every high escape velocity simulation are twofold. In addition to the fact that winds are more compressed and are launched deeper in the planet's potential well, another consequence of a small scale height is that a small change in $R_{\rm min}$ results in a large change in pressure. This means that, following our prescription for the calculation of lower boundary conditions (Appendix B), raising the pressure of $R_{\rm min}$ by, say, a factor of 10 results in a very small change in radius (e.g., lowering from $R_{\rm min} = 1.04 R_P$ to just 1.03 R_P) and an order-of-magnitude change in $\rho(R_{\rm min})$. Large changes in $\rho(R_{\rm min})$ are numerically costly and likely to fail. In addition, the resultant change in radius may still not be sufficient to capture the actual photoionization base, $R_{\rm XUV}$. Thus, modeling the lower portion of the upper atmosphere in the high escape velocity limit remains an area of ongoing exploration.

5.2. Low Escape Velocity Limit

The low escape velocity limit presents its own set of challenges related to the lower boundary of the simulation (those at the border of or within the hatched region of Figures 9 and 10). For low escape velocity planets, the large scale height means that `Wind-AE` finds $R_{\rm XUV}$ to be extremely high in the atmosphere (up to $8 R_P$ for super-Earths modeled).

This elevated $R_{\rm XUV}$ occurs regardless of whether the bolometric heating/cooling and molecular layer prescription are turned on. When they are turned on, however, the magnitudes of bolometric heating/cooling terms (which are a function of density) often naturally decline with radius (i.e., not as a result of the enforced decline of the complementary error function that enforces the molecular-to-atomic transition) before reaching $R_{\rm XUV}$. This means that there is no longer an isotherm in the molecular region below the wind and the resulting thermal inversion can dip several hundred kelvin below $T_{\rm skin}$ (e.g., from 1200 to 1000 K; see, e.g., Figure 18).

While this thermal inversion is neither unphysical nor unexpected, it may require the inclusion of additional physics, making the ability of our model to be easily coupled to more sophisticated lower-atmosphere models especially valuable in these cases. These inclusions may consist of more carefully treating the infrared and optical opacities used in the bolometric heating and cooling calculations. They may also consist of adding molecular line cooling terms, since the low, nonisothermal temperature in the region below the wind (M. Schulik & R. A. Booth 2023; W. Misener et al. 2025) may mean that molecules do not thermally dissociate or photodissociate and are present throughout the region and into the wind.

In some of the most extreme cases, the sonic point ($R_{\rm bolo,sp}$) for bolometrically driven mass loss (i.e., core-powered mass loss or boil-off) is of order $R_{\rm XUV}$. This means that XUV photons may not be the predominant driver of the wind and, indeed, they may be absorbed in the supersonic portion of an outflow and be unable to contribute to the heating of the wind because a supersonic flow is not causally connected. This regime is usually referred to as core-powered mass loss or boil-off, depending on the point in a planet's evolution at which this phenomenon is occurring. J. E. Owen & H. E. Schlichting (2023) mapped out this parameter space analytically, showing that both occur for expected planet properties; however, detailed numerical simulations like ours are required before the combined mass-loss rates are used in evolutionary models. These underdense planets may also be in the regime where Roche lobe overflow is a significant contributor to mass-loss rates (e.g., N. V. Erkaev et al. 2007; B. Jackson et al. 2017).

We do not include planets where $R_{\rm bolo,sp} < R_{\rm XUV}$ in our grid, but we do include some planets for which $R_{\rm sp} > R_{\rm Hill}$, the Hill sphere (hatched region in Figure 9; see also Appendix Figure 18 for a profile of such a planet). While an isothermal Parker wind does not allow for the sonic point to be outside of the planet's Hill sphere, a nonisothermal solution with a positive temperature gradient past the Hill sphere (through the sonic point) does (e.g., H. J. G. L. M. Lamers & J. P. Cassinelli 1999). We test our analytical boundary condition prescription against a more sophisticated multilayer interior model that includes, e.g., more detailed bolometric radiative transfer (Y. Tang et al. 2025) and find that we match the microbar radius computed by the interior model. This agreement indicates that these planets are indeed incredibly puffy and potentially on the verge of core-powered mass loss. Given that planets with low escape velocities in our grids have incredibly high mass-loss rates, it is also likely that these mass–radius combinations (overlap of the hatched region and colored region in Figures 9 and 10) would not exist in nature for such highly irradiated planets, as they would have likely undergone a short and violent period of boil-off or core-powered mass loss early in their lives. Even if these mass–radius combinations did exist, for the level of bolometric and XUV irradiation our grids, these planets may not be stable for long, with the incredibly high mass-loss rates stripping significant fractions of their remaining atmospheres. Detailed simulations of the transition between the core-powered and photoevaporation mass-loss regimes (J. E. Owen & H. E. Schlichting 2023) merit further investigation.

5.3. Additional Physics

Within the molecular layer below the wind, there may be a thin region toward the top of the layer that is still optically thin to heating by the highest-energy X-ray photons but is likely cooled by H_{3+} molecular line emission (R. V. Yelle 2004; A. García Muñoz 2007). This means that heat deposited by high-energy photons in the molecular region below the wind will be largely removed by radiative and/or bolometric cooling, meaning that the contributions of the highest-energy X-rays to the outflows may be negligible.

Explicitly modeling the H_3^+ cooling requires more nuanced and expensive photochemical calculations than are sensible in a relaxation model, but we can approximate the effects of H_{3+} cooling by cutting off the high-energy end of the stellar spectrum at 165 eV and reducing the flux above 70 eV by 70% as found by Frelikh et al. (submitted). The differences in outflow structure and $\dot{M}$ are negligible for a 2.02 $M_\oplus$ 5.3 $R_\oplus$ H–He planet when compared to the same planet irradiated by a full XUV spectrum (13.6–2000 eV) when both planets have fluxes normalized to 13.6–40 eV. Since the highest-energy X-rays are already being absorbed below the wind in a H–He atmosphere, they already contribute minimally to the direct heating of the outflow and contribute negligibly to puffing up the atmosphere below the wind when compared to the contributions of bolometric heating. Hence, the absence of the highest-energy photons (>165 eV) when "removed" by our pseudo–H_{3+} cooling has minimal impact. For winds containing metals, this choice will be more important.

At the top of the hypothetical X-ray-heated and H_{3+}-cooled layer, molecules are ultimately thermally dissociated and the outflow is atomic, so we elect to treat the molecular layer holistically as a region with constant mean molecular weight, whose energy budget is predominantly set by bolometric heating and cooling. As we noted in the previous section, though, these assumptions break down for small planets that may have a different thermal or molecular–atomic fraction structure.

5.4. Summary of Comparison to Other Work

To first order, the results of our benchmarking can be broken down as follows. In the high-flux limit differences in the outflow energetics prove important, and in the low-flux limit differences in SED shape and lower boundary modeling have the largest impact. The primary source of differences between our model and the high X-ray flux model (J. E. Owen & A. P. Jackson 2012) is our inclusion of Lyα and *PdV* cooling. As a result, we find higher mass-loss rates for planets with higher escape velocities and lower ones for lower escape velocities than the high X-ray flux grids in J. E. Owen & A. P. Jackson (2012).

An advantage of our model is the ability to model both the high (as above) and low incident stellar flux limit with the same physics. In the low-flux limit, we explore several case studies. In keeping with previous findings that emphasize the impact of stellar spectral shape, profile differences between our model and those of A. García Muñoz (2007; HD 209458 b, H–He), D. Kubyshkina et al. (2024; GJ 1214 b, H–He), and A. Caldiroli et al. (2022; HD 209458 b, H–He) can be attributed primarily to the differences in the input stellar spectra. Likewise, the good agreement with M. Salz et al. (2016; HD 209458 b, H) we attribute to the similarities in the spectra.

The other major source of differences is the lower boundary conditions. Our approximation of the region below the wind as molecular and dominated by bolometric heating/cooling represents an improvement over models that scale directly from the planetary transit radius, and this approximation results in a much higher altitude $R_{\rm XUV}$ and significantly different outflow profile (A. Gillet et al. 2023; $0.05M_{\rm J}$, $0.55R_{\rm J}$, H–He). However, in comparison to a model with more sophisticated lower-atmosphere modeling (C. Huang et al. 2023; WASP-121b, metals), we find a much lower $R_{\rm XUV}$. Notably, when we match the spectrum and lower boundary conditions to those in the incredibly comprehensive and more expensive C. Huang et al. (2023) model, we are able to closely reproduce their profile and mass-loss rates in less than $1/100$ of the time.

6. Summary

We built on the 1D photoionization-driven steady-state hydrodynamic transonic Parker wind relaxation code developed by R. A. Murray-Clay et al. (2009) by adding metal and X-ray physics, as well as a Python wrapper that aids in ramping through the relaxation code solution space, in performing post facto calculations, in smoothing input stellar spectra, and in visualizing solutions. A fast-forward model allows us to perform broad parameter space studies smoothly across such parameters as stellar flux (Figures 9 and 3), planet size (Figure 8), semimajor axis (Figure 7), spectral ranges (Figures 5 and 4), presence of metals (Figure 6), and, in the future, metallicity.

The speed and versatility of `Wind-AE` allow it to be applied to explore a number of open problems. `Wind-AE`'s Python interface and open-source nature allow it to be easily coupled with chemical network codes that model atmosphere behavior below the optically thin upper atmosphere and with interior models and XUV spectrum evolution codes in order to model planetary evolution due to atmospheric escape.

Acknowledgments

The authors thank the referee for thoughtful comments. This paper makes use of the following Python libraries: `numpy` (C. R. Harris et al. 2020), `matplotlib` (J. D. Hunter 2007), and `scipy` (P. Virtanen et al. 2020).

M.I.B., R.M.-C., and J.R.M. acknowledge funding support from NSF CAREER grant 1663706. M.I.B. and R.M.-C. acknowledge support from NASA'S Interdisciplinary Consortia for Astrobiology Research (NNH19ZDA001N-ICAR) under grant No. 80NSSC21K0597 and from NASA XRP grant No. 80NSSC23K0282. J.E.O. is supported by a Royal Society University Research Fellowship. This project has received funding from the European Research Council (ERC) under the European Union's Horizon 2020 research and innovation program (grant agreement No. 853022). We acknowledge use of the Lux supercomputer at UC Santa Cruz, funded by NSF MRI grant AST 1828315. We would like to thank Chenliang Huang for sharing data; Linda Lewis for time evolution discussions; Jorge Fernandez-Fernandez, Emerson Tao, and Artem Aguichine for beta testing `Wind-AE`; and Ethan Schreyer and Sarah Blunt for Hill sphere discussions, and Yao Tang for boundary condition confirmation.

Software: `Wind-AE` is available on Github (https://github.com/mibroome/wind-ae). Data for all plots can be found in the Notebooks subdirectory (https://github.com/mibroome/wind-ae/tree/main/Notebooks/).

Appendix A
Comparisons to Existing Results

Here we benchmark our model against a selection of the other numerical models in the literature. For all of the comparisons herein, we continue to use a scaled solar spectrum from a low-activity period of the Sun and use the physical boundary conditions for the outflow discussed in Section 2 unless otherwise specified. It is important to note that a number of models use different geometric surface averaging schemes for the mass-loss rate, so instead of reporting $\dot{M} = 0.3 \cdot 4\pi R_{\rm sp}^2 \rho(R_{\rm sp}) v(R_{\rm sp})$ as in the main body of the text, here we report $\dot{M}_{/f} = \dot{M}/f = 4\pi R_{\rm sp}^2 \rho(R_{\rm sp}) v(R_{\rm sp})/f$, where f is a factor between 1 and 4. This allows us to make direct comparisons to mass-loss rates found in models in the literature that use different geometric averaging factors. We consider the mass-loss rates to be in agreement if they fall within 30% of each other.

One of the advantages of `Wind-AE`'s relative speed is that we are able to reproduce the results of more expensive models, including those coupled with full photochemical lower-atmosphere models. The model in A. García Muñoz (2007) is one such well-known model. It is a 1D multifrequency EUV hydrodynamic model that uses a photochemical network to model photoionization of hydrogen down to $r = R_P$ and includes conductive and H3+ cooling, but not Lyα cooling. For a pure-H HD 209458 b, we find good agreement in the outflow structure and mass-loss rate (Figure 11) when we employ the same high-activity EUV solar spectrum used by A. García Muñoz (2007; see also P. G. Richards et al. 1994), turn off Lyα line cooling, and match lower boundary conditions (Figure 11). We normalize the spectrum to $F_{\rm tot} = 2474\,{\rm erg\,s^{-1}\,cm^{-2}}$ over the range of 12–165 eV, where the upper bound is chosen to simulate the effect of H_3^+ cooling that radiates away the highest-energy photons.

Notably, we get relatively poor agreement with the same flux, same wavelength range, but different solar spectrum (the lower-activity `FISM2` spectrum used in the main body of the text). This is consistent with the findings of, e.g., J. H. Guo & L. Ben-Jaffel (2016), D. Kubyshkina et al. (2024), and M. Schulik & J. Owen (2025a), who report that SED shape can have a significant influence on the outflow physics. In particular, we find that a higher flux or different SED shape in low-energy (<60 eV) EUV photons results in a shallower temperature gradient and warmer outflow at high radii. This appears to be the result of a larger flux of low-energy photons being absorbed at $\tau({\rm EUV}) = 1$ surfaces at high fluxes.

We also benchmark against other relatively fast and simple 1D substellar models such as A. Caldiroli et al. (2022; ATES). ATES is a 1D multifrequency XUV H–He steady-state Godunov-type

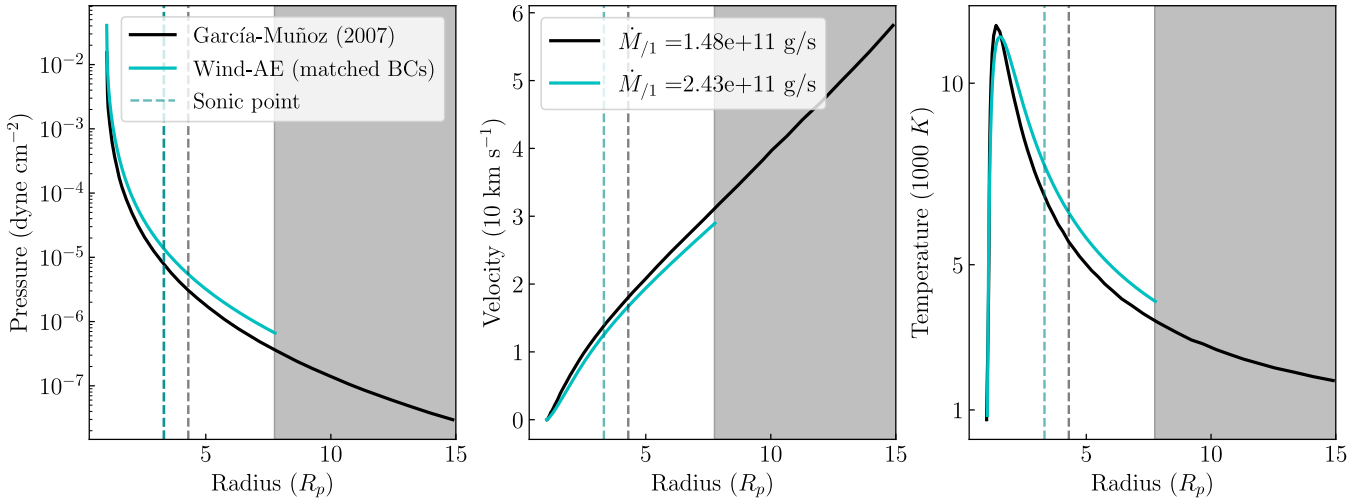

Figure 11. HD 209458 b pure H (A. García Muñoz 2007). We reproduce the SP solution of Figures 3–4 in A. García Muñoz (2007) for an EUV-irradiated pure-H atmosphere (black). The Wind-AE solution plotted (cyan) is for a pure-H atmosphere with no Lyα cooling, a similar if not identical high-activity solar spectrum ($F_{\rm tot}$ = 2474 erg s^{-1} cm^{-2} integrated over 13.6–165 eV, which loosely simulates H3+ cooling), and BCs matched to those of the black solution ($R_{\rm min}$ = 1.03 R_P, T = 730 K, $\rho = 5.82 \times 10^{-13}$ g cm^{-3}). Sonic points are dashed lines, and the solid gray region is the Coriolis radius past which our model is not valid.

hydrodynamic code. ATES models similar ionization and heating/cooling sources to `Wind-AE`, but ATES also includes free–free and collisional heating/cooling and does not include secondary ionizations (all of which are negligible for HD 209458 b with a H–He atmosphere; R. A. Murray-Clay et al. 2009). ATES includes advection in post-processing, which limits the accuracy of ionization profiles for low-flux planets but still produces accurate outflow rates. The post-processing step also currently requires manual intervention, resulting in a slightly longer runtime than our model.

For the comparison in Figure 12, we run ATES for HD 209458 b and set the ATES boundary conditions to match the physical BCs computed for the base of the simulation by `Wind-AE`: $\log_{10}(n_0) = 13.04$, $T_{\rm eq} = 1535$ K, and H/He number ratio = 0.0629. ATES employs a power-law estimate for the stellar SED (A. Caldiroli et al. 2022), so to match the total flux and the ratio of X-ray to EUV flux, we set the log X-ray luminosity in ATES to 26.89 and log EUV luminosity to 27.8. This difference in SED is the source of the steeper temperature gradient at higher radii and the lower velocity in the ATES profile. The two models are otherwise in good agreement, and ATES takes a similar amount of CPU time, but longer wall time, to run.

We also compare to the L. A. Dos Santos et al. (2022) `p-winds`, a 1D multifrequency steady-state XUV isothermal Parker wind backward model with multispecies capabilities, including line cooling, but not including the X-ray physics detailed in Section 2.3. Because `p-winds` is isothermal, it is incredibly computationally inexpensive, but not a comparable model to the nonisothermal ones listed in this section. We set the input $\dot{M}$ to `p-winds` equal to the $\dot{M}_{/3} = 2.1 \times 10^{10}$ g s^{-1} computed by `Wind-AE` and the input isothermal temperature equal to the temperature at the peak of `Wind-AE`'s temperature profile (T = 8616 K). `p-winds` does not converge for isothermal temperature equal to the average temperature (T = 3561 K) of our model. For the `p-winds` solution, we employ `p-winds`'s default solar spectrum without any modifications, meaning that integrated flux over 13.6–2000 eV is $F_{\rm tot}$ = 1342 erg s^{-1} cm^{-2} versus the $F_{\rm tot}$ = 1095 erg s^{-1} cm^{-2} in `Wind-AE`. The results for a H–He atmosphere (0.8:0.2 mass fraction, 0.94:0.6 number fraction) are shown in Figure 12. Depending on how close in parameter space `Wind-AE`'s initial guess is and the number of metals present in the wind, `p-winds` either runs in a similar time or is up to 1000 times faster.

ATES, `p-winds`, and `Wind-AE` all make simplifying assumptions to avoid the expense of non-LTE photochemical computation; however, several 1D models employ the 1D multispecies photoionization solver CLOUDY (G. J. Ferland et al. 2017) to handle the gas microphysics and photochemistry within the outflow and/or below the wind. D. Linssen et al. (2024; Sunbather) integrate CLOUDY and `p-winds`, D. Kubyshkina et al. (2024; CHAIN) integrate CLOUDY and D. Kubyshkina et al. (2018b), and M. Salz et al. (2016; TPCI) integrate CLOUDY and the 3D MHD model PLUTO (A. Mignone et al. 2012). We compare to the GJ 1214 b outflow profiles from D. Kubyshkina et al. (2024) for the latter two here. TPCI is the PLUTO–CLOUDY interface, a steady-state 1D multifrequency XUV, multispecies solver, and contains the same ionization and heating/cooling terms as `Wind-AE` and also free–free, conductive, and collisional heating/cooling (which are negligible for GJ 1214 b). Our outflow profiles are in good agreement for HD 209458 b with a pure-H atmosphere (Figure 13) with 1D structure differences likely stemming from differences in the Lisird low-activity Sun spectrum used (M. Salz et al. 2016). As in `Wind-AE`, TPCI is able to self-consistently compute the heating efficiency.

CHAIN contains the same ionization and heating sources as TPCI and, additionally, includes H_3^+ cooling and secondary ionizations through CLOUDY (D. Kubyshkina et al. 2024). We model GJ 1214 b with the parameters listed in Table 1 of D. Kubyshkina et al. (2024) and with the scaled solar spectrum with integrated flux $F_{\rm tot}$ = 886 erg s^{-1} cm^{-2} for the range 13.6–2000 eV (Figure 14). D. Kubyshkina et al. (2024) attribute the differences from TPCI in the GJ 1214 b outflow profiles to differences in the stellar spectra that each model used, resulting in different heating in the lower atmosphere. Despite significant temperature profile differences likely

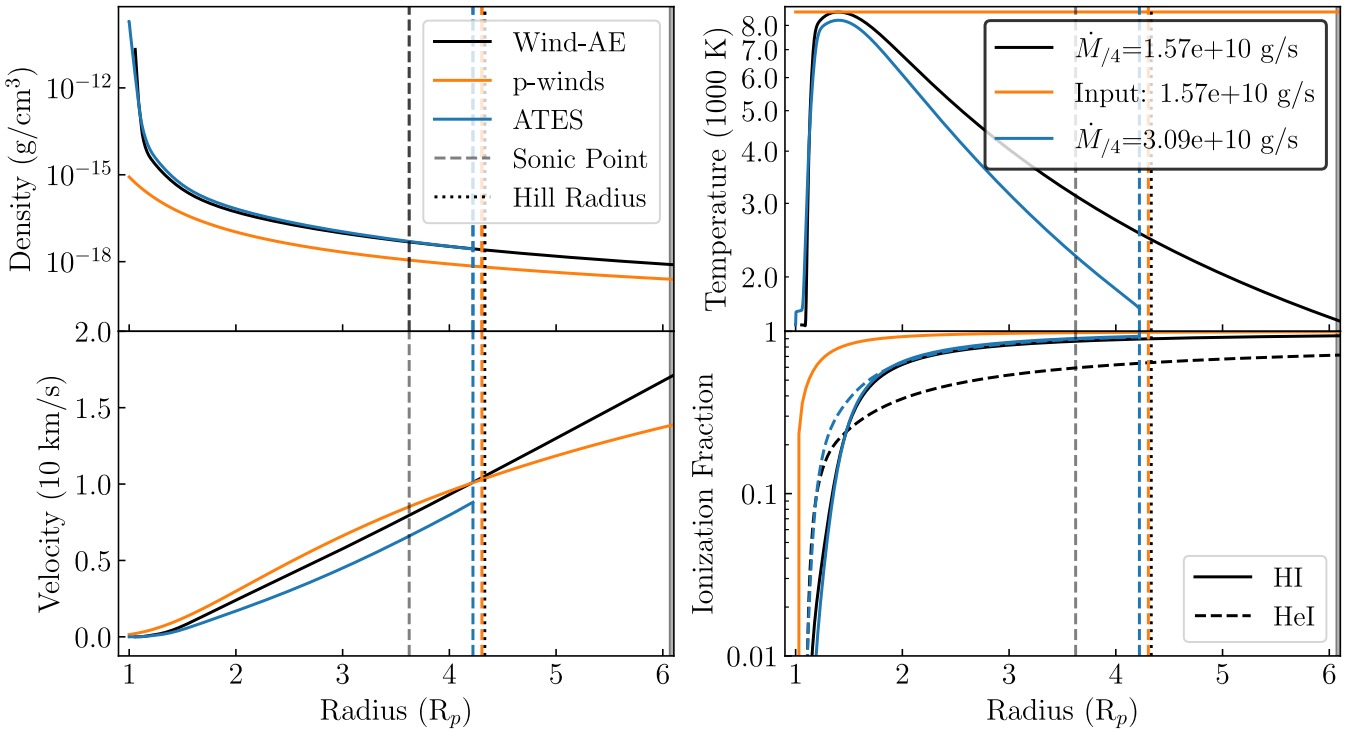

Figure 12. HD 209458 b H–He comparisons with ATES and `p-winds`–`Wind-AE` H–He (black), ATES H–He (blue, A. Caldiroli et al. 2022), and `p-winds` pure-H (orange; L. A. Dos Santos et al. 2022) profiles for HD 209458 b. Inputs to `p-winds` are $T = 8616$ and $\dot{M} = 1.57 \times 10^{10}$ g s^{-1} (the $\dot{M}_{/4}$ computed by `Wind-AE`). Sonic points are plotted as dashed vertical lines, and the Hill radius is plotted as a dotted vertical line. All three employ different approximations to solar spectra.

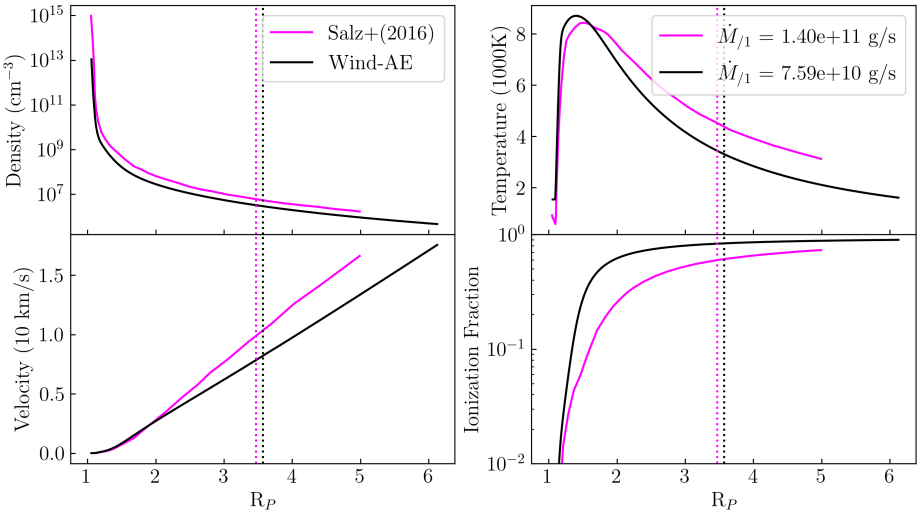

Figure 13. Pure-H HD 209458 b TPCI model (M. Salz et al. 2016; TPCI, magenta), with lower BCs of $T(R_{\rm min}) = 1000$ K, $R_{\rm min} \sim 1.05 R_P$, $\rho(R_{\rm min}) \sim 1.6 \times 10^{-9}$ g cm^{-3}. We have confirmed that these boundary conditions are not the source of the profile differences.

stemming from SED differences, we find good agreement with $\dot{M}_{/1} = 1.58 \times 10^{11}$ g s^{-1}. We confirm that lower boundary condition differences are not the source of structure differences for both TPCI and CHAIN. This is consistent with our findings for other low-flux hot Jupiters.

Our lower boundary conditions do turn out to make a significant impact on the profile of WASP-121b when compared with C. Huang et al. (2023; see also Figure 14). This model uses the T. T. Koskinen et al. (2022) atmospheric escape model (an update of T. T. Koskinen et al. 2013) with a photochemical hydrostatic model 100 bars and 1 μbar, where the escape model takes over. This model is extremely comprehensive and includes diffusion, drag, charge exchange, thermal ionizations, and a variety of other nuanced physics calculations that our model does not include. When we use the bolometric heating/cooling and molecular layer to compute the lower boundary conditions as in the main body of this text, `Wind-AE` produces the lime-green profile and $\dot{M}_{/4} = 8.45 \times 10^{11}$ g s^{-1} in Figure 15 for an atmosphere that consists of H I, He I, C I, N I, O I, S I, Mg II, Si II, Ca II, and Fe II. To eliminate spectral differences as the source of any discrepancies, we use the same spectrum as C. Huang et al. (2023).

Notably, when we manually set our lower boundary conditions to match Case B of C. Huang et al. (2023; H I,

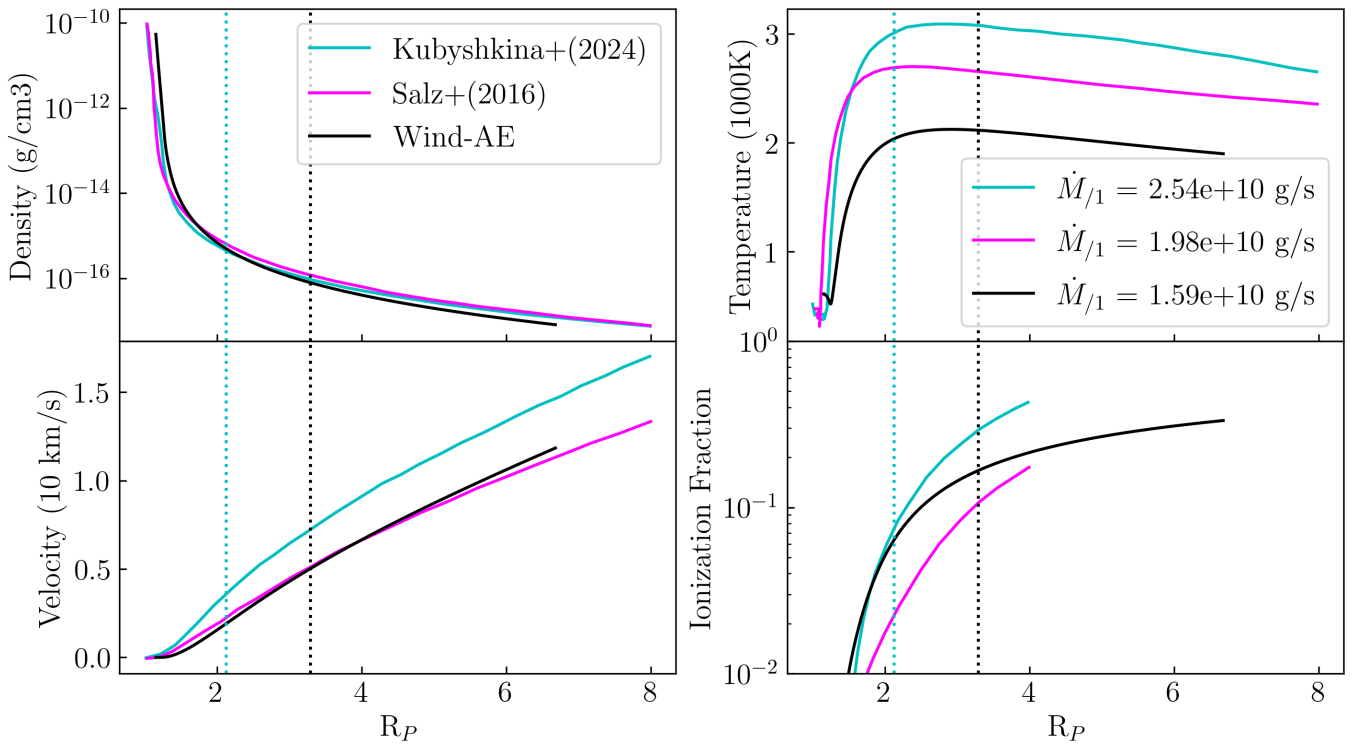

Figure 14. H–He GJ 1214 b CHAIN and TPCI models—GJ 1214 b: 6.36 $M_{\oplus}$, 2.69 $R_{\oplus}$, 0.014 au, 0.18 $M_{\odot}$, 3.51 × $10^{-3}L_{\odot}$, 886 erg s^{-1} cm^{-2}. The D. Kubyshkina & L. Fossati (2022) CHAIN solar spectrum solution (cyan) and M. Salz et al. (2016) TPCI solution (magenta) are reproduced here.

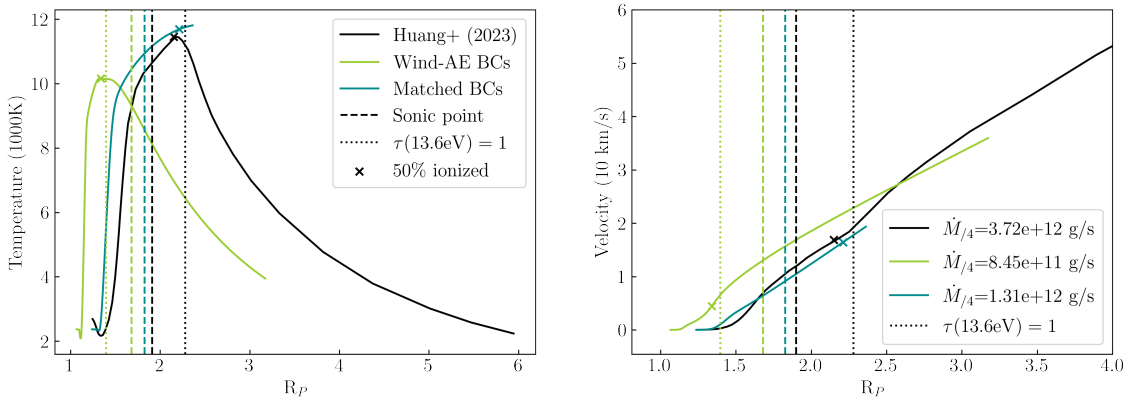

Figure 15. Metals WASP-121b (C. Huang et al. 2023)—WASP-121b: 1.18M_J, 1.77R_J, 0.03 au, 1.35 $M_{\odot}$, 2.6 $L_{\odot}$, $F_{\rm tot}$ = 6.66 × 10^4 erg s^{-1} cm^{-2}. Case B (C. Huang et al. 2023, Figure 20) with solar abundances of H I, He I, C I, N I, O I, S I, Mg II, Si II, Ca II, Fe II, K I, and Na I is reproduced in black. `Wind-AE` models for solar abundances of all of the above species except Fe II, K I, and Na I using our lower BCs (green) and matching BCs (blue) of $R_{\rm min}$ = 1.24 and $\rho(R_{\rm min})$ = 1.39 × 10^{-11} g cm^{-3} are plotted. Both also have the same input stellar spectrum as the black solution does.

He I, C I, N I, O I, S I, Mg II, Si II, Ca II, Fe II, K I, and Na I), we are able to compute a profile and mass-loss rate ($\dot{M}_{/4} = 1.3 \times 10^{12} g \quad s^{-1}$) similar to that found by C. Huang et al. (2023; $\dot{M}_{/4} = 3.7 \times 10^{12}$ g s^{-1}) in less than 1/100 of the computational time.

HD 209458 b and GJ 1214 b are old, low-flux planets whose mass loss is in the energy-limited regime and dominated by EUV flux, with the presence of X-rays having relatively little effect on pure-H and H–He atmospheres. Outflows in the high-flux limit, on the other hand, are considered recombination limited; young stars exhibit a higher proportion of higher X-ray flux relative to the bolometric and EUV flux; and Lyα cooling becomes more significant. To test our model in the high-flux limit, we compare to two high XUV flux models, the first of which is J. E. Owen & A. P. Jackson (2012).

We model a H–He atmosphere for a 1.72R_J, 1M_J planet and a 5R_J, 1M_J planet at 0.1 au around a solar-type star with an X-ray luminosity of 10^{30} erg s^{-1} to compare outflow profiles with those in Figure 4 of J. E. Owen & A. P. Jackson (2012). We scale our solar spectrum such that the flux in the X-ray between 100 and 2000 eV corresponds to $L_X = 10^{30}$ erg s^{-1}. The net EUV flux between 13.6 and 2000 eV is then $F_{\rm tot} = 3.57 \times 10^5$ erg s^{-1} cm^{-2}. J. E. Owen & A. P. Jackson (2012) make the simplifying assumption that the outflow is in ionization equilibrium, which is valid in the high XUV flux limit where the outflow is "recombination limited." As a result,

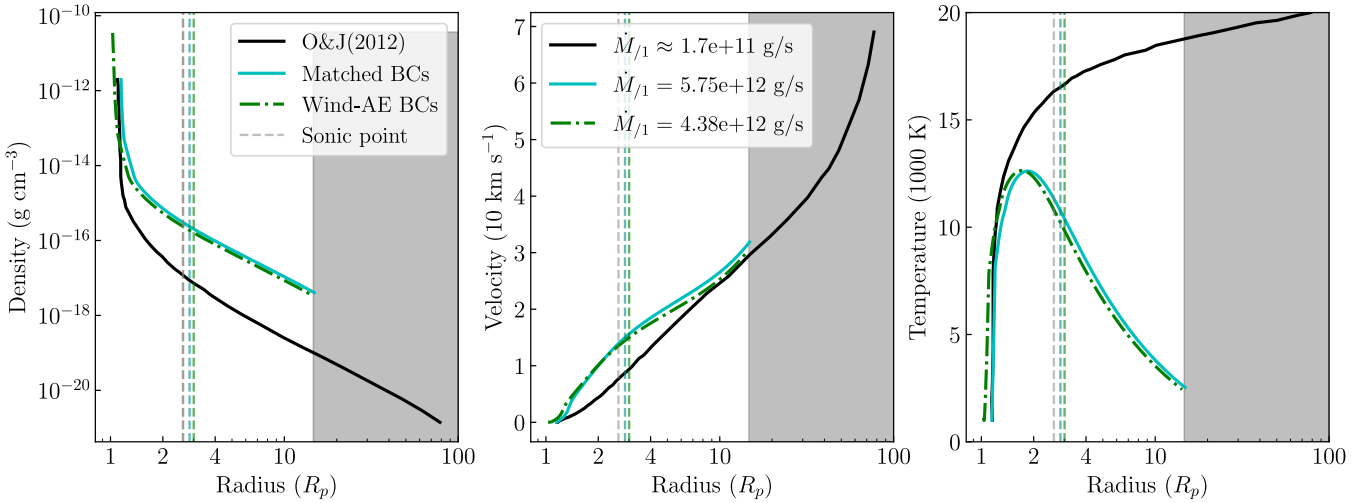

Figure 16. Profiles for planets in the high X-ray flux limit—reproduction of Figure 4 in J. E. Owen & A. P. Jackson (2012; black), a model that does not contain *PdV* or Lyα cooling. Density, velocity, and temperature results are given for a $1M_J$, $1.73R_J$ (dark) and $5R_J$ (light) planet at 0.1 au irradiated by a 1 $M_\odot$ star with X-ray luminosity $L_X = 10^{30}$ erg s^{-1} cm^{-2}. Wind-AE profiles are plotted for planets with physical BCs (green) and BCs that match the BCs of the black solution (cyan). To match $L_X = 10^{30}$ ergs cm^{-2}, our planets are irradiated by a scaled solar spectrum of total flux 13.6–2000 eV of 3.57×10^5 erg s^{-1} cm^{-2}. Sonic points are plotted as dashed vertical lines.

the J. E. Owen & A. P. Jackson (2012) analytic solution is not frequency dependent, making our choice of a scaled modern-day solar spectrum adequate for the purposes of comparing—though attempts to model a planet around a young XUV-active star should take into account the higher ratio of X-ray flux to EUV flux for younger stars.

With the inclusion of Lyα cooling and *PdV* cooling, and solving the ionization balance equation, we find that the outflow is much cooler at high altitudes and stays much denser throughout (Figure 16). Even when we remove the bolometrically heated/cooled molecular layer and match the lower boundary temperature and density of J. E. Owen & A. P. Jackson (2012), these features remain. As a result, we predict higher geometrically averaged mass-loss rates ($\dot{M}_{/3}$) for planets with higher escape velocities and lower mass-loss rates for lower escape velocities than predicted in the J. E. Owen & A. P. Jackson (2012) mass-loss grid (Figure 17).

Figure 18 provides a further illustration of the importance of the lower boundary conditions in determining outflow structure. We match the outflow structure of a low escape velocity planet modeled by A. Gillet et al. (2023; black) when we match their boundary conditions (yellow). However, when we take into account bolometric heating and cooling, the planet is significantly inflated, generating a very different outflow structure. Relative to results that do not employ lower-atmosphere models, our boundary condition implementation finds significantly higher R_{XUV} for low escape velocity planets (Figure 18).

The lower-atmospheric model included in C. Huang et al. (2023) is more sophisticated than that used by default in `Wind-AE`. The fact that `Wind-AE` provides an excellent match to this work's outflow structure if and only if the lower boundary conditions are matched (Figure 15) indicates that modeling the region below the wind as a simple energetic balance between bolometric heating and cooling with a fixed mean molecular weight has the potential to underestimate the

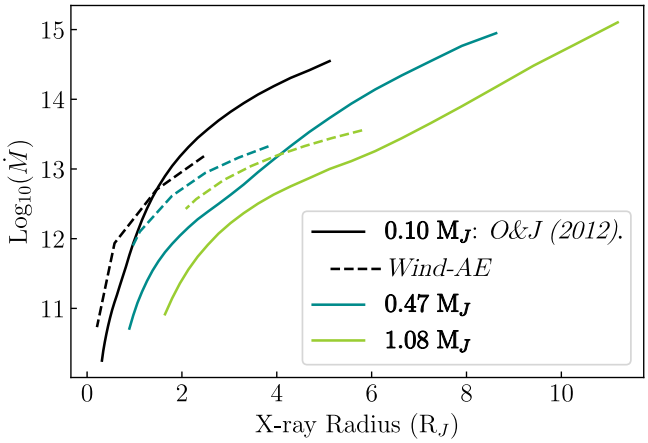

Figure 17. J. E. Owen & A. P. Jackson (2012) mass-loss grid. Solid lines are slices at $0.1M_J$ (black), $0.47M_J$ (dark cyan), and $1.08M_J$ (green) through the mass-loss grid for planets at 0.1 au irradiated by a 1 $M_\odot$ star with X-ray luminosity $L_X = 10^{30}$ erg cm^{-2} from Figure 5 in J. E. Owen & A. P. Jackson (2012). Note that the radii in that figure are not optical transit radii but the approximate $\tau(1\text{ keV}) = 1$ radius. Hence, we plot the log of geometrically averaged $\dot{M}_{/3}$ in g s^{-1} as a function of $\tau(1\text{ keV}) = 1$ for planets of the same masses (dashed). The dashed solutions do not extend to higher X-ray radii because planets with higher R_P values enter the low escape velocity regime, in which the relaxation code is currently not well characterized (see Section 5.2).

microbar radius and thereby the wind launch radius (R_{XUV}). Fortunately, `Wind-AE` can be easily coupled to lower-atmosphere models whose outputs of radius, density, temperature, metal abundances, ionization fractions, mean molecular weight, etc., can be easily fed as inputs into `Wind-AE`. The default lower-atmosphere model in `Wind-AE` is nevertheless an improvement over setting boundary conditions at a fixed multiple of the optical transit radius and is valuable for increasing the accuracy of R_{XUV} when more sophisticated lower-atmospheric modeling is not available.

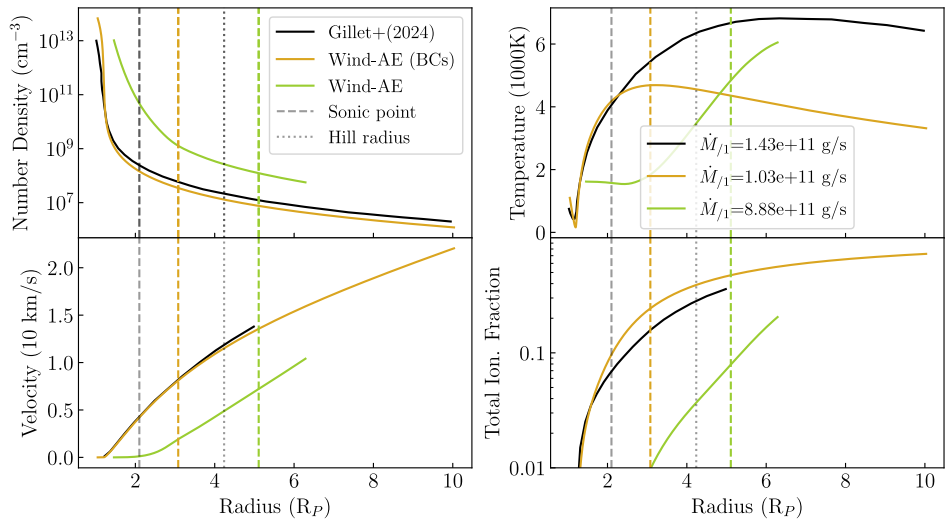

Figure 18. A. Gillet et al. (2023) secondary ionization profiles. We reproduce profiles from Figure 7 in A. Gillet et al. (2023) for a $0.05M_J$, $0.55R_J$ planet at 0.045 au around a solar-type star for a pure-H outflow modeled using PLUTO with secondary ionizations enabled (black). `Wind-AE` profile for the same planet with the same solar spectrum plotted, but with bolometric heating and cooling and $\mu = 2.3m_H$ for $r < R_{XUV}$ enabled (green) and without (yellow). Yellow boundary conditions at $R_{min} = 1.1R_P$ are matched to black ($T = 1100$K, $\rho = 1.326 \times 10^{-10}$ g s^{-1}, $P = 12$ μbar), while green use Wind-AE's default lower BCs.

Appendix B
Boundary Conditions

The upper boundary condition, the sonic point, R_{sp}, is where $v(R_{sp}) = c_s(R_{sp})$. This is a natural critical point that emerges from the transonic Parker wind solution (see R. A. Murray-Clay et al. 2009, Equations (15)–(16)). A discussion of the lower boundary conditions follows.

B.1. Bolometric Heating and Cooling

Though the molecular layer below $\sim 10^{-9}$ bars is optically thick to most XUV radiation, it can still be heated by the bolometric flux from the star, which peaks in the optical. The bolometric heating and cooling naturally enforce an isotherm at the skin temperature below the wind (we do not model molecular line cooling by, e.g., H_{3+}). The balance of bolometric heating and cooling allows us to analytically estimate more physical lower boundary condition values at R_{min}.

We select the lower boundary condition such that the majority of the flux is captured in the wind. For computational efficiency, we choose this to be the 1 μbar radius, but the pressure is customizable. The $\tau(\nu) = 1$ surface for the highest-energy photons ($\gtrsim$1 keV) is below 1 μbar; however, we find the contributions of these highest-energy photons to the mass-loss rates in typical systems to be negligible. If one is concerned with modeling more precise ionization fractions of a species as a function of radius, one may set the base of the simulation to a higher pressure.

The balance between thermal emission and incident stellar bolometric radiation sets the skin temperature, T_{skin}, in the region below the wind and above the $\tau_{IR} = 1$ surface. Above nanobar pressures, the molecules are photodissociated and become atomic in the wind for most planets (though super-Earths may be the exception (see Frelikh et al., submitted). Within the wind, photoionization heating, Lyα cooling, and *PdV* cooling dominate, setting the temperature of the wind throughout the flow.

The addition of bolometric heating and cooling to this investigation allows the relaxation code to physically solve for where the photoionization heating begins to dominate and the wind launches. Since the $\tau(\nu) = 1$ surfaces will be different for photons of different frequencies, ν, and will depend on the metallicity and metals present (via the ionization cross section, $\sigma_s(\nu)$; see Figure 20), estimating the radius of the wind base is nontrivial. Additionally, the mass-loss rate and wind structure are sensitive to the pressure where the wind is launched, because deeper penetration tends to lead to cooler, slower winds with lower mass-loss rates (see Figure 4).

To set the T_{skin} isotherm below the wind, the bolometric flux, $F_* = \frac{L_*}{4\pi a^2}$, is computed from the bolometric luminosity, L_*, and semimajor axis, a. The skin temperature (Equation (B4)) is obtained by setting the optically thin bolometric heating, Γ_{bolo} (taken as the sum of direct and indirect bolometric heating), and bolometric cooling, Λ_{bolo}, equal,

$$\Gamma_{bolo} = F_{in,opt}\kappa_{opt}\rho(r) + F_{in,IR}\kappa_{IR}\rho(r) \tag{B1}$$

$$= F_*\rho(r)\left(\kappa_{opt} + \frac{1}{4}\kappa_{IR}\right), \tag{B2}$$

$$\Lambda_{bolo} = 2\sigma_{SB}T_{skin}^4\rho(r)\kappa_{IR}, \tag{B3}$$

where $F_{in,opt} = F_*$ captures the direct bolometric heating from the star and $F_{in,IR} = \sigma_{SB}T_{eq}^{1/4} = \frac{1}{4}F_*$ is via the gray slab approximation for reemission of IR radiation. Then, using the fact that R_P for most planets given is the *slant path* optical surface, we can solve geometrically using $\tau_{slant,opt} = \kappa_{opt}l\rho(R_P) = 1$, where l is the slant path length of stellar optical photons through the transiting planet's atmosphere. To first order, $l = \sqrt{8H_{sc}R_P}$, where the scale height H_{sc} is computed using the skin temperature and mean *molecular* weight (as opposed to atomic, as is usually the case in the wind). The default adjustment for the mean molecular weight is a factor of 2.3 to account for molecular hydrogen, but users have the ability to customize this value and are recommended to do so for more metal-rich atmospheres.

B.2. Computing Lower Boundary Temperature, Radius, and Density

The skin temperature then becomes

$$T_{\rm skin} = \left[\frac{F_*(\kappa_{\rm opt} + \kappa_{\rm IR}/4)}{2\sigma_{\rm SB}\kappa_{\rm IR}}\right]^{1/4}. \quad \text{(B4)}$$

The exact prefactors in this equation are dependent on geometry and various Eddington coefficients, but the impact of their exact choice is small, thanks to the quartic root. In Equation (B4), $\kappa_{\rm opt} = 0.004$ and $\kappa_{\rm IR} = 0.01$ are the defaults for optical and infrared opacity, respectively. These values are no longer valid in the atomic, optically thin wind, so we multiply by an error function to drop $\kappa_{\rm opt}$ and $\kappa_{\rm IR}$ to zero in the wind. Between the base of the wind and the $\tau_{\rm IR} = 1$ radius the atmosphere is an isotherm at the skin temperature.

Density at R_P is then

$$\rho(R_P) = \sqrt{\frac{\mu_{\rm mol} G M_P}{8 R_P^3 k_{\rm B} T_{\rm skin} \kappa^2_{\rm opt}}}. \quad \text{(B5)}$$

For most planets, the pressure at R_P is of order 10 mbars. However, to ease the computational burden, either we place the bottom of the simulation at 1 μbar, or, if the $\tau_{\rm IR} = 1$ surface to vertically incident photons $R_{\rm IR}$ is above R_P, we take the base of the simulation to be $R_{\rm IR}$. Most XUV rays are absorbed between micro- and nanobar pressures, with winds launching approximately around the 10 nanobar radius. At higher pressures than microbar pressures, the balance of bolometric heating and cooling enforces an isotherm at the skin temperature.

Because the $\kappa_{\rm opt}$ and $\kappa_{\rm IR}$ should drop off as the molecules are thermally dissociated and photodissociated and the mean molecular weight should transition to the atomic (Figure 19), we need a way to enforce this transition occurring before the wind launches at $R_{\rm XUV}$. To do so, we use a complementary error function, normalized so that its values limit to 1 and 0, because it allows us to modify the rate and location of the drop-off as appropriate for a given profile:

$$x = \frac{v(r) - v_{R_{\rm XUV}}}{k H_{sc,0} \frac{\Delta v}{\Delta r}|_{R_{\rm XUV}}}$$
$$\text{erfc}'(x) \equiv \frac{\text{erfc}(x)}{\text{erfc}(x)|_{\rm max}}, \quad \text{(B6)}$$

where v is the local comoving velocity as a function of r, $v_{R_{\rm XUV}}$ is the velocity at $R_{\rm XUV}$, and $\Delta v/\Delta r$ is the slope of the velocity in the vicinity of $R_{\rm XUV}$, so that x is only a function of r. Here we elect to use velocity as a function of radius because the steep acceleration from $0\,{\rm cm\,s^{-1}}$ when the wind launches results in a complementary error function that drops to zero when the wind begins to accelerate at $R_{\rm XUV}$. Then, $xH_{\rm sc,0} = x\frac{k_{\rm B}T(R_{\rm XUV})R^2_{\rm XUV}}{\mu_{\rm mol} G M_P}$ is some multiple k of the scale height at $R_{\rm XUV}$, where $R_{\rm XUV}$ is computed as the radius at which photoionization heating begins to dominate over PdV cooling. This creates an error function that drops from 1 to 0 over k scale heights at $R_{\rm XUV}$. The default value of k is 1. The altitude in the atmosphere at which these high-energy photons are absorbed (where $\tau(\nu) = 1$) depends on the frequency ν of the incident photon. We compute $R_{\rm XUV}$ and radial extent of the complementary error function post facto as part of the process of polishing the relaxation solution to self-consistency. As such, $R_{\rm XUV}$ is not affected by our choices for Equation (B6).

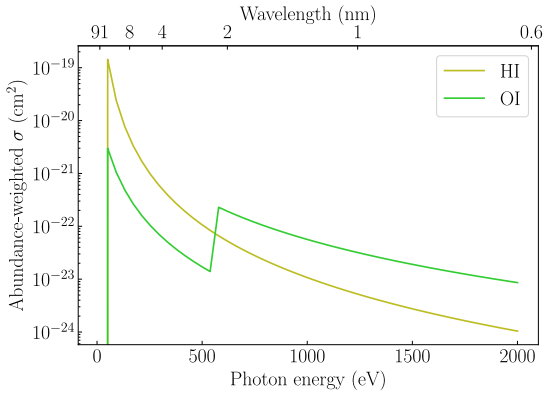

Figure 19. Abundance-weighted ionization cross sections—photoionization cross sections for H I (olive) and O I (lime green) weighted by their fractional abundance (0.79332 and 0.00669, respectively) at 1× solar metallicity as a function of photon energy (bottom axis) and wavelength (top axis). Frequency-dependent cross sections are derived from coefficients and analytic equations in D. A. Verner & G. J. Ferland (1996) and I. M. Band et al. (1990).

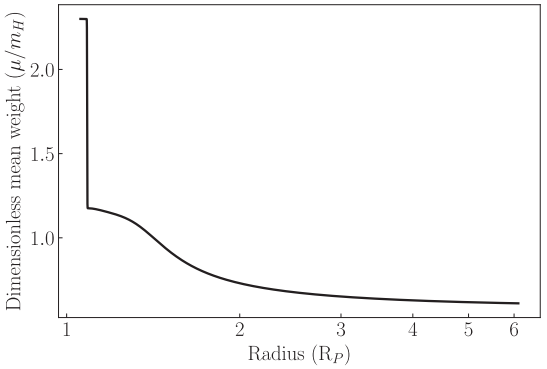

Figure 20. Mean weight complementary error function transition—the transition from mean molecular weight $\mu(r < R_{\rm XUV}) = 2.3 m_{\rm H}$ to mean atomic weight as governed by Equation (14) for HD 209458 b. Here the erfc decays over 1 scale height at $R_{\rm XUV}$.

To compute the simulation lower boundary radius, $R_{\rm min}$, and density, $\rho(r = R_{\rm min})$, we use the hydrostatic equilibrium equation and the assumption of isothermality of the region between $R_{\rm IR}$ and the wind base to derive

$$R_{\rm min}(P_{R_{\rm min}}) = \left[\frac{c_s^2}{GM_P}\ln\left(\frac{P_{R_{\rm min}}}{P(R_P)}\right) + \frac{1}{R_P}\right]^{-1} \quad \text{(B7)}$$

$$\rho(R_{\rm min}) = P_{R_{\rm min}}\frac{\mu_{\rm mol}}{k_{\rm B}T_{\rm skin}}, \quad \text{(B8)}$$

where $P(R_P)$ is the pressure at R_P and $P_{R_{\rm min}}$ is the pressure at the base of the simulation, both in barye (10^{-6} bars). This value should always be between 1 μbar and 1 mbar to capture the contributions from the highest-energy photons and to stay in the isothermal portion of the atmosphere.

For our assumptions of $T(R_{\rm min}) = T_{\rm skin}$ to be reasonable, the atmosphere should be isothermal and hydrostatic between R_P and $R_{\rm min}$. The safest way to guarantee that our $R_{\rm min}$ falls within that isothermal region would be to set $R_{\rm min} \geqslant R_{\rm IR}$ to $\tau_{\rm IR} = 1$ radius to vertically incident IR photons. Notably, $R_{\rm IR}$ is

typically below R_P, the optical slant path radius of the planet in transit. As such, `Wind-AE` has a rarely activated condition that, should $R_{\rm IR} > R_P$, $R_{\rm min} = R_{\rm IR}$, and we can similarly solve from hydrostatic equilibrium to obtain

$$R_{\rm IR} = \frac{R_P^2}{H_{\rm sc} \ln\left(\frac{\rho(R_{\rm IR})}{\rho(R_P)} e^{R_P/H_{\rm sc}}\right)}, \tag{B9}$$

where we approximate the scale height at $R_{\rm IR}$ to be the scale height at R_P and $\rho(r = R_{\rm IR})$ follows from $\tau_{\rm IR} = \rho(R_{\rm IR})\kappa_{\rm IR} H_{\rm sc} = 1$.

B.3. The High Escape Velocity Limit: $R_{\rm min} > R_{\rm XUV}$

In high escape velocity cases and low-flux cases such as those discussed in Section 5.1, a larger fraction of XUV photons are absorbed below $R_{\rm min}(1\ \mu{\rm bar})$, so setting the base at $R_{\rm min}(1\ \mu{\rm bar})$ does not capture $R_{\rm XUV}$. The correct approach would be to set $R_{\rm min}$ to a higher pressure in order to accurately capture the radius at which the wind launches. However, because of the small scale height for these planets, this approach is computationally costly and the relaxation method can fail. Therefore, in our model we opt to turn off the bolometric heating/cooling and other molecular layer assumptions, because that layer is not captured at $R_{\rm min}(1\ \mu{\rm bar})$.

Indeed, the assumptions we make to derive our lower boundary conditions are no longer valid, and holding $T(R_{\rm min}) = T_{\rm skin}$ results in numerical temperature oscillations with radius. Instead, because $R_{\rm min}$ does not capture the true base of the wind, $T(R_{\rm min})$ should be several thousand kelvin higher than $T_{\rm skin}$. Taking the average of the first five radial numerical temperature oscillations near the simulation base gives us a decent estimate of what the $T(R_{\rm min})$ should be for this $R_{\rm min}$ located in the middle of the wind.

We confirm that this approximation is adequate by lowering the simulation base to, e.g., $R_{\rm min}(100\ \mu{\rm bar})$, so that we accurately capture the molecular region and $R_{\rm XUV}$ and compare our oscillation-averaged temperature at 1 μbar in the shallow solution to the actual temperature at $R(1\ \mu{\rm bar})$ in the deeper solution (Figure 21). The density should also slightly change in this case, but we find that the effects of changing $\rho(R_{\rm min})$ to a more physically accurate value are secondary. In the highest escape velocity limits, setting $R_{\rm min}(1\ \mu{\rm bar})$ and using the above method to find $T(R_{\rm min})$ is no longer sufficient, as the planets' scale heights are so small that the region below $R_{\rm min}(1\ \mu{\rm bar})$ is dense enough to absorb higher-energy X-rays that contribute to heating and ionizing; thus, we may be underestimating temperature and ionization fraction at $R_{\rm min}(1\ \mu{\rm bar})$, as well as the total mass-loss rate.

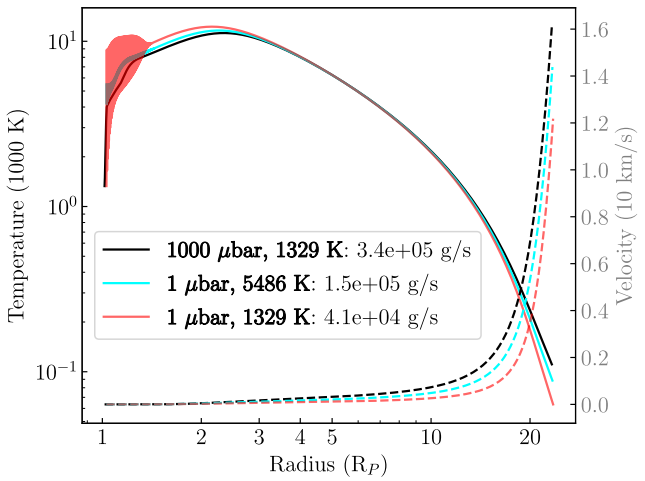

Figure 21. Smoothing high escape velocity planet lower BC temperature oscillations—55 $M_\oplus$, 1.85 $R_\oplus$ at 0.05 au with $F_{\rm tot} = 1095$ erg s^{-1} cm^{-2} temperature (right y-axis, solid) and velocity profiles (left y-axis, dashed). For a lower boundary pressure of 1 μbar, $R_{\rm min} = 1.028R_P$, which does not capture the bolometrically heated/cooled region, so $T(R_{\rm min}(1\mu{\rm bar})) \neq T_{\rm skin} = 1324$ K (red) and results in an order-of-magnitude-higher mass loss than the ground truth (black). Averaging the temperature oscillations tells us the $T(R_{\rm min}(1\mu{\rm bar})) = 5486$ K (cyan), which puts the mass-loss rate within a factor of 2. Because neither of these solutions captures the molecular region, there is no higher mean molecular weight or bolometric heating/cooling included. To confirm the validity of this approximation, we lower (black) the base pressure to 1000 μbar ($R_{\rm min} = 1.016R_P$) to capture the photoionization base and molecular region, thus making $T(R_{\rm min}(1000\mu{\rm bar})) = T_{\rm skin} = 1324$ K.

Appendix C
Escape of Lyα Photons

The planetary winds modeled here are optically thick to Lyα radiation since, at line center, the cross section for Lyα absorption by a neutral hydrogen atom is larger than the cross section for photoionization. Nevertheless, as illustrated in R. A. Murray-Clay et al. (2009, their Appendix C), the wind is low enough in density that the majority of Lyα photons emitted in the wind ultimately scatter into the line wings and escape before their energy can be returned to the thermal bath. An Lyα photon's energy is thermalized if it excites an atom and the atom then experiences a collision, resulting in collisional de-excitation, before the atom has the chance to spontaneously de-excite and reemit another Lyα photon.

To validate the order-of-magnitude calculation in R. A. Murray-Clay et al. (2009), we run a Monte Carlo calculation of Lyα photon escape. We use the hot Jupiter profile for a H–He HD 209458 b provided in Figure 8 and assume spherical symmetry. We run 1000 photons, each beginning at radius $r = 1.18R_p$, where the Lyα cooling rate peaks for this outflow. At each step in the calculation, we draw a random direction and an Lyα frequency, ν, from a Voigt profile at the local temperature and density, Doppler-shifted

into the inertial frame according to the flow velocity, $v_{\parallel}$, along the drawn direction at the point of emission. We use the integrated optical depth along that direction,

$$\int n_{0,\mathrm{H}}(r)\sigma_{\mathrm{abs}}(\nu, r, v_{\parallel})dl, \tag{C1}$$

to draw a random distance at which the photon is absorbed. The number density of neutral hydrogen, $n_{0,\mathrm{H}}$, and the cross section for absorption at frequency ν, $\sigma_{\mathrm{abs}}(\nu)$—which depends through the Voigt profile on temperature and density—are both functions of the radial coordinate r. We note that, given the chosen direction, the variation of r along the path is determined by geometry. Because our photon frequency is chosen in the inertial frame, the cross section is also a function of the local bulk velocity along the chosen direction, $v_{\parallel}$, evaluated at each r.

Once the photon is absorbed, we calculate, using gas conditions at its new radial distance, the timescale t_{col} on which it is expected to be de-excited by collision with an electron (cross section $2 \times 10^{-15}\,\mathrm{cm}^2$; R. T. Brackmann et al. 1958), a proton (cross section $2 \times 10^{-14}\,\mathrm{cm}^2$ including charge exchange; G. Hunter & M. Kuriyan 1977), or other species. For other species, we use the electron cross section, which is a reasonable approximation for typical collisions with a neutral hydrogen atom. More detailed treatment of individual species is not merited because electron collisions dominate. Given a spontaneous decay rate of $A_{21} = 6.265 \times 10^8\,\mathrm{s}^{-1}$ for hydrogen Lyα, the probability that the photon is thermalized before reemission is $1 - e^{-1/(A_{21}t_{\mathrm{col}})} \approx (A_{21}t_{\mathrm{col}})^{-1}$. We draw a random number to determine whether the photon is thermalized at this step. Because our example wind profile transitions to the bolometrically heating regime below $1.1R_p$ and we do not trust detailed model conditions below this radius, we treat any photon that reaches a radius smaller than $1.1R_p$ as having escaped from our modeled flow. The energy from these photons may be radiated away by bolometric or molecular radiation at depth, or they may be thermalized at depth, heating the gas below our simulation region and contributing to the physical processes that determine appropriate lower boundary conditions for our simulations. We consider a photon to have escaped the wind outward into space if it reaches a radius of $10R_p$.

We find that 72.4% of our modeled photons escaped the wind outward to space and 27.5% were lost through the lower boundary, with only 0.1% thermalized in our simulation domain, demonstrating that a majority of the photons indeed escape. We reran the calculation starting photons at $1.11R_p$, near the base of the wind simulation where Lyα excitation via secondary electrons is most important. Though this starting point is very near to our autothermalization distance, 52.2% of the 1000 modeled photons escaped outward to space, 47.5% escaped through the lower boundary, and 0.3% were thermalized in the simulation domain.

In examples with higher incident flux, Lyα cooling is typically more important. We therefore repeated this calculation for a planet with the same mass and radius but an incident flux 100 times larger. We found that photons emitted from the peak of the Lyα cooling region escaped outward 65.6% of the time, escaped through the lower boundary 33.4% of the time, and were thermalized in the domain 1% of the time. For this example, no bolometric heating region is modeled, and photons started just above the lower boundary of the simulation escaped outward 40.1% of the time and inward 59.3% of the time, with 0.6% of photons thermalized in the domain.

In both cases, a majority of the Lyα cooling radiation indeed escapes from the outflow. For secondary electron energy that goes into Lyα excitation, the ultimate escape fraction depends on the true fate of photon energy that diffuses below the base of our simulation. As discussed in Section 2.3.3, our choice to treat this energy as escaping does not make a substantial difference to our results.

Appendix D
Multispecies and Multifrequency Versions of Finite-difference Equations

To solve for Equations (1)–(5), we update Equations (9)–(13) of R. A. Murray-Clay et al. (2009) to include our multispecies and multifrequency assumptions:

$$\begin{aligned} E_{1,j} &\equiv \Delta_j\rho - \frac{d\rho}{dr}\Delta_j r \\ &= \Delta_j\rho + \rho\left(\frac{2}{r} + \frac{1}{v}\frac{dv}{dr}\right)\Delta_j r = 0 \end{aligned} \tag{D1}$$

$$\begin{aligned} E_{2,j} &\equiv \Delta_j v - \frac{dv}{dr}\Delta_j r \\ &= \Delta_j v - \frac{v}{v^2 - \gamma\lambda kT/\mu} \\ &\quad \times \left[\frac{2\gamma\lambda kT}{\mu r} - \frac{(\gamma-1)Q}{\rho v} - \frac{GM_P}{r^2} + \frac{GM_*}{(a-r)^2}\right. \\ &\quad \left. + \frac{1}{2}\frac{GM_*(a - r(1 + M_P/M_*))}{a^3}\right]\Delta_j r = 0 \end{aligned} \tag{D2}$$

$$\begin{aligned} E_{3,j} &\equiv \Delta_j T - \frac{dT}{dr}\Delta_j r \\ &= \Delta_j T - \left[(\gamma-1)\left(\frac{Q}{\rho v}\frac{\mu}{k} + \frac{T}{\rho}\frac{d\rho}{dr}\right) + \frac{T}{\mu}\frac{d\mu}{dr}\right] = 0 \end{aligned} \tag{D3}$$

$$\begin{aligned} E_{4+s,j} &\equiv \Delta_j\Psi_s + \frac{d\Psi_s}{dr}\Delta_j r \\ &= \Delta_j\Psi_s - \frac{m_s}{Z_s\rho v}(\mathcal{R}_s - \mathcal{I}_s)\Delta_j r = 0 \end{aligned} \tag{D4}$$

$$\begin{aligned} E_{(4+N_{\mathrm{sp}})+s,j} &\equiv \Delta_j N_{\mathrm{col}} - \frac{dN_{\mathrm{col}}}{dr}\Delta_j r \\ &= \Delta_j N_{\mathrm{col}} + \Psi_s\frac{Z_s\rho}{m_s}\Delta_j r = 0, \end{aligned} \tag{D5}$$

where j is the point along the radial grid, $Q = \Gamma + \Lambda$, and Z_s is the mass fraction of species s. We write N_{sp} as shorthand for N_{species}, the number of species, s, in the wind, where s is in the range of $[0, N_{\mathrm{species}} - 1]$. Therefore, the number of equations in the system of equations becomes $3+2N_{\mathrm{species}}$, hence the computational expense of modeling more metals.

The final equation is given in terms of $N_{\mathrm{col},s}$, rather than τ as in R. A. Murray-Clay et al. (2009), because $\tau_\nu = \sum_s \sigma_{\nu,s}N_{\mathrm{col},s}$ and individual species may ionize at different rates as a function of radius, so we must track the column density of each species individually in order to calculate τ.

The most important changes are summarized here. For a more detailed discussion of numerical and analytic changes, see J. McCann (2021).

Appendix E
Spectrum

We avoid the cost of running a high-resolution spectrum by fitting a polynomial to the input stellar spectrum. Any observed spectrum—such as the FISM2 solar spectrum from the LISIRD database we use for this paper—or realistic simulated XUV spectrum will vary widely in flux and shape across the spectral range, as well as be high in resolution, making fitting polynomials difficult. If the spectral qualities can be well approximated by low-degree polynomial(s), though, it is inexpensive to accurately perform numerical integrations using Gauss–Legendre quadrature. Thus, we use the smoothing and binning algorithm (discussed in more detail in J. McCann 2021, Section 2.3.5).

Logarithmic fits and/or the least-squares method would not locally (or, potentially, even globally) conserve energy along the spectrum; thus, we employ a Savitzky–Golay filter, which smooths evenly spaced noisy data with a rolling polynomial. First, we smooth the peaks and troughs of the spectrum by passing the spectrum multiple times through the Savitzky–Golay filter. The effect of running a Savitzky–Golay filter on small segments is similar to running a single-pass filter on a larger wavelength range, but it distorts the data less than a standard, larger single-pass filter and better preserves the area under the smoothed spectrum. The filtered spectrum is then renormalized to conserve total energy in each bin. Next, a fifth-degree polynomial is fit to the filtered spectrum, again rescaling to preserve energy in each bin. The polynomial is calculated by using a spline with an infinite smoothing factor, which relaxes the spline to a single bin interval.

Binning the spectrum allows us to run the multipass filtering in fewer smoothing passes and allows us to more accurately preserve the spectrum shape, especially at the ionization wavelengths of species present in the model. Subbinning, in particular, allows us to fit the spectrum with more low-order polynomials, as opposed to fewer polynomials that would have to be higher order and would be more difficult to accurately and cheaply integrate using Gauss–Legendre quadrature. For our bins, we choose bin width $2r$ centered at wavelength λ_0 such that the error over $\lambda \in [\lambda_0 - r, \lambda_0 + r]$ is less than ϵ. Using the analytic D. A. Verner & G. J. Ferland (1996) cross section relations, we can take the logarithmic derivatives of the Verner cross sections $\sigma_{\lambda,s}$ for species s and use the chain rule to derive the bin half-width,

$$r \leqslant \left(\frac{6\epsilon}{||\sigma^{(3)}_{\lambda,s}||_\infty} \right)^{1/3}. \tag{E1}$$

Bin edges are also placed at the ionization energies and K-shell ionization energies of the species present, unless one of the ionization energies of an existing species is within 2 nm of an existing species' ionization energy.

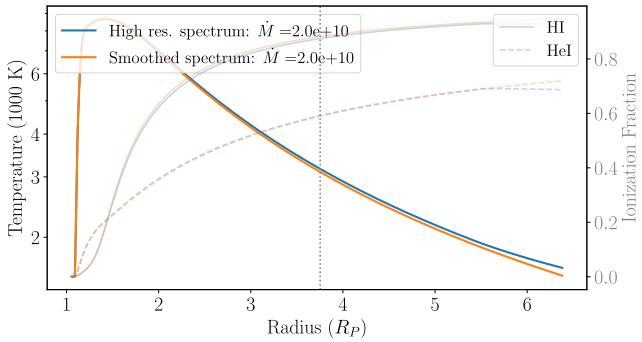

Figure 22. High-resolution scaled solar spectrum versus smoothed. Shown in blue are solutions using the FISM2 LISIRD solar spectrum scaled to an integrated flux of 1095 erg s^{-1} cm^{-2}, and shown in orange are solutions using the smoothed spectrum normalized to the same integrated flux (as in Figure 2). Thicker, darker lines are the temperature profile, and thinner, lighter lines are the ionization fraction.

The physical effects of smoothing a spectrum are also mitigated by using the above method. Ionizing energy is conserved since the peaks of the spectrum are smoothed and distributed locally—meaning that there will be an equal amount of photons higher and lower than the peak ionization energy in the wind. That being said, at the edges of the spectrum, where there are not necessarily symmetric peaks over which to smooth, this method may over- or underestimate the number of higher- or lower-energy photons. As Figure 22 shows, the effects on the outflow are minimal for the XUV solar spectrum, so we take this smoothed approximation for a high-resolution spectrum to be sufficient for our work.

Appendix F
Metal Line Cooling

The metal line cooling rates for C II, C III, O II, and O III are computed via the emissivity equation (Equation (17)), where A' in that equation is the correctly scaled version of A such that Λ is the cooling rate per unit volume. CLOUDY (G. J. Ferland et al. 2017) is then used to compute the coefficients A, $T_{\rm line}$ (line transition temperature), and n_c (critical number density) in Tables 1, 2, 3, and 4.

We use CHIANTI (K. P. Dere et al. 1997; G. Del Zanna et al. 2015) to identify all the relevant lines and extract the values that are listed below. These fits provide total cooling rates that are typically good to 10%–30% and at worst a factor of two in extreme regions of the parameter space. We show a comparison of the two-level model fits compared to the numerical solution, including all the energy levels and transitions (still under the assumption of a statistical collisional equilibrium) for O II in Figure 23, demonstrating the fit's accuracy in the temperature range of interest.

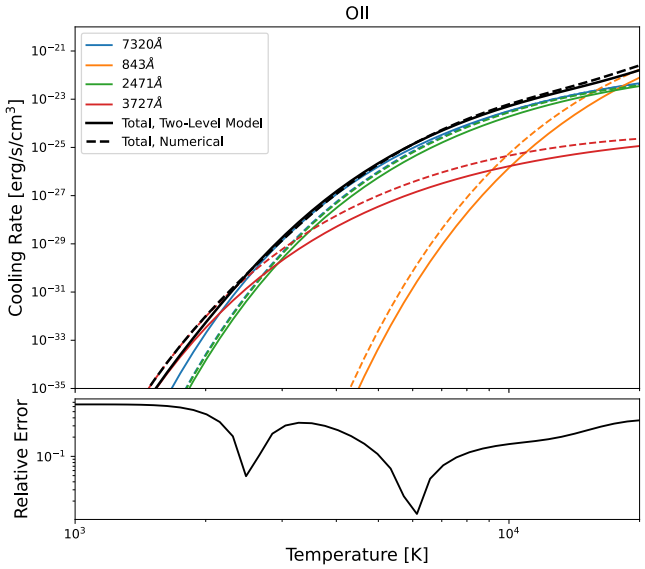

Figure 23. Top: the colored lines show a comparison of our two-level atom model fits to the cooling rates (solid) against the numerically computed cooling rates (dashed) for the individual transitions of O II. The black lines show a comparison of the two-level model for the four most relevant lines compared to the full numerical cooling rate including all the energy levels and transitions (still under the assumption of a statistically collisional equilibrium). The lines are shown for an electron density of 5.4556×10^8 cm^{-3}. Bottom: the relative error between the total cooling rate computed from our two-level atom approach and the total numerically computed cooling rate, demonstrating that our accuracy is at the 10%–30% level in the temperature range of interest.

Table 1
Properties for the Cooling Functions of C II–All Values in cgs Units

Line	A'	$T_{\rm line}$	n_c
157 μm	1.783E–20	91.2	1.388E+01
2326 Å	1.215E–10	61853.9	1.210E+09
1334 Å	2.413E–03	107718.1	3.740E+15

Table 2
Properties for the Cooling Functions of C III—All Values in cgs Units

Line	A'	$T_{\rm line}$	n_c
1910 Å	3.84E–10	75460.8	1.314E+9
977 Å	1.791E–03	147263.9	7.172E+14

Table 3
Properties for the Cooling Functions of O II—All Values in cgs Units

Line	A'	$T_{\rm line}$	n_c
843 Å	5.786E–4	172421.6	1.322E15
2471 Å	3.812E–13	58225.3	4.488E7
3727 Å	4.299E–16	38575.0	5.365E3
7320 Å	3.769E–13	53063.6	3.110E7

Table 4
Properties for the Cooling Functions of O III—All Values in cgs Units

Line	A'	$T_{\rm line}$	n_c
52 μm	3.138E–18	277.682	2.549E3
5000 Å	3.387E–14	28728.6	9.667E5
166 Å	6.560E–10	86632.4	1.476E10
83.5 Å	1.752E3	172569.7	5.406E21

ORCID iDs

Madelyn I. Broome https://orcid.org/0000-0002-7520-5663
Ruth Murray-Clay https://orcid.org/0000-0001-5061-0462
John R. McCann https://orcid.org/0000-0002-5155-6645
James E. Owen https://orcid.org/0000-0002-4856-7837

References

Affolter, L., Mordasini, C., Oza, A. V., Kubyshkina, D., & Fossati, L. 2023, A&A, 676, A119
Allan, A., & Vidotto, A. A. 2019, MNRAS, 490, 3760
Asplund, M., Grevesse, N., Sauval, A. J., & Scott, P. 2009, ARA&A, 47, 481
Band, I. M., Trzhaskovskaia, M. B., Verner, D. A., & Iakovlev, D. G. 1990, A&A, 237, 267
Biassoni, F., Caldiroli, A., Gallo, E., et al. 2024, A&A, 682, A115
Brackmann, R. T., Fite, W. L., & Neynaber, R. H. 1958, PhRv, 112, 1157
Caldiroli, A., Haardt, F., Gallo, E., et al. 2022, A&A, 663, A122
Cecchi-Pestellini, C., Ciaravella, A., & Micela, G. 2006, A&A, 458, L13
Chadney, J. M., Galand, M., Unruh, Y. C., Koskinen, T. T., & Sanz-Forcada, J. 2015, Icar, 250, 357
Chamberlin, P. C., Eparvier, F. G., Knoer, V., et al. 2020, SpWea, 18, e02588
Dalgarno, A., Yan, M., & Liu, W. 1999, ApJS, 125, 237
Del Zanna, G., Dere, K. P., Young, P. R., Landi, E., & Mason, H. E. 2015, A&A, 582, A56
Dere, K. P. 2007, A&A, 466, 771
Dere, K. P., Landi, E., Mason, H. E., Monsignori Fossi, B. C., & Young, P. R. 1997, A&AS, 125, 149
Dos Santos, L. A., Alam, M. K., Espinoza, N., & Vissapragada, S. 2023, AJ, 165, 244
Dos Santos, L. A., Vidotto, A. A., Vissapragada, S., et al. 2022, A&A, 659, A62
Edwards, B., Changeat, Q., Tsiaras, A., et al. 2023, AJ, 166, 158
Ehrenreich, D., Bourrier, V., Wheatley, P. J., et al. 2015, Natur, 522, 459
Ercolano, B., & Clarke, C. J. 2010, MNRAS, 402, 2735
Erkaev, N. V., Kulikov, Y. N., Lammer, H., et al. 2007, A&A, 472, 329
Erkaev, N. V., Lammer, H., Odert, P., et al. 2016, MNRAS, 460, 1300
Ferland, G. J., Chatzikos, M., Guzmán, F., et al. 2017, RMxAA, 53, 385
Fossati, L., Ayres, T. R., Haswell, C. A., et al. 2013, ApJL, 766, L20
Friedrich, M. M., Mellema, G., Iliev, I. T., & Shapiro, P. R. 2012, MNRAS, 421, 2232
García Muñoz, A. 2007, P&SS, 55, 1426
Gillet, A., Munoz, A. G., & Strugarek, A. 2023, A&A, 680, 16
Guillot, T. 2010, A&A, 520, A27
Guo, J. H., & Ben-Jaffel, L. 2016, ApJ, 818, 107
Habing, H. J., & Goldsmith, D. W. 1971, ApJ, 166, 525
Harris, C. R., Millman, K. J., van der Walt, S. J., et al. 2020, Natur, 585, 357
Huang, C., Arras, P., Christie, D., & Li, Z.-Y. 2017, ApJ, 851, 150
Huang, C., Koskinen, T., Lavvas, P., & Fossati, L. 2023, ApJ, 951, 123
Hunten, D. M., Pepin, R. O., & Walker, J. C. G. 1987, Icar, 69, 532
Hunter, G., & Kuriyan, M. 1977, RSPSA, 353, 575
Hunter, J. D. 2007, CSE, 9, 90
Jackson, A. P., Davis, T. A., & Wheatley, P. J. 2012, MNRAS, 422, 2024
Jackson, B., Arras, P., Penev, K., Peacock, S., & Marchant, P. 2017, ApJ, 835, 145
Kempton, E. M. R., & Knutson, H. A. 2024, RvMG, 90, 411

Kempton, E. M. R., Zhang, M., Bean, J. L., et al. 2023, Natur, 620, 67
King, G. W., & Wheatley, P. J. 2020, MNRAS: Letters, 501, L28
King, G. W., & Wheatley, P. J. 2021, MNRAS, 501, L28
Kirk, J., Ahrer, E.-M., Claringbold, A. B., et al. 2025, MNRAS, 537, 3027
Koskinen, T. T., Harris, M. J., Yelle, R. V., & Lavvas, P. 2013, Icar, 226, 1678
Koskinen, T. T., Lavvas, P., Huang, C., et al. 2022, ApJ, 929, 52
Kubyshkina, D., & Fossati, L. 2022, A&A, 668, A178
Kubyshkina, D., Fossati, L., & Erkaev, N. V. 2024, A&A, 684, A26
Kubyshkina, D., Fossati, L., Erkaev, N. V., et al. 2018a, ApJ, 866, L18
Kubyshkina, D., Lendl, M., Fossati, L., et al. 2018b, A&A, 612, A25
Kubyshkina, D. I., & Fossati, L. 2021, RNAAS, 5, 74
Lamers, H. J. G. L. M., & Cassinelli, J. P. 1999, Introduction to Stellar Winds (Cambridge Univ. Press)
Lammer, H., Stökl, A., Erkaev, N. V., et al. 2014, MNRAS, 439, 3225
Lecavelier Des Etangs, A., Ehrenreich, D., Vidal-Madjar, A., et al. 2010, A&A, 514, A72
Lee, E. J., & Connors, N. J. 2021, ApJ, 908, 32
Linssen, D., Shih, J., MacLeod, M., & Oklopčić, A. 2024, A&A, 688, 17
Linssen, D. C., & Oklopčić, A. 2023, A&A, 675, A193
Loyd, R. O. P., Schreyer, E., Owen, J. E., et al. 2025, Natur, 638, 636
Malsky, I., & Rogers, L. A. 2020, ApJ, 896, 48
McCann, J. 2021, PhD thesis, UC Santa Barbara (https://escholarship.org/uc/item/0qc1m9zn)
McCann, J., Murray-Clay, R. A., Kratter, K., & Krumholz, M. R. 2019, ApJ, 873, 89
Mignone, A., Zanni, C., Tzeferacos, P., et al. 2012, ApJS, 198, 7
Misener, W., Schulik, M., Schlichting, H. E., & Owen, J. E. 2025, ApJ, 980, 152
Murray-Clay, R. A., Chiang, E. I., & Murray, N. 2009, ApJ, 693, 23
Nortmann, L., Pallé, E., Salz, M., et al. 2018, Sci, 362, 1388
Osterbrock, D. E., & Ferland, G. J. 2006, Astrophysics of Gaseous Nebulae and Active Galactic Nuclei (Univ. Science Books)
Owen, J. E. 2019, AREPS, 47, 67
Owen, J. E. 2020, MNRAS, 498, 5030
Owen, J. E., & Alvarez, M. A. 2016, ApJ, 816, 34
Owen, J. E., & Jackson, A. P. 2012, MNRAS, 425, 2931
Owen, J. E., Murray-Clay, R. A., Schreyer, E., et al. 2023, MNRAS, 518, 4357
Owen, J. E., & Schlichting, H. E. 2023, MNRAS,
Owen, J. E., & Wu, Y. 2016, ApJ, 817, 107
Owen, J. E., & Wu, Y. 2017, ApJ, 847, 29
Pai Asnodkar, A., Wang, J., Broome, M., et al. 2024, MNRAS, 535, 1829
Parmentier, V., & Guillot, T. 2014, A&A, 562, A133
Parmentier, V., Guillot, T., Fortney, J. J., & Marley, M. S. 2015, A&A, 574, A35
Penzlin, A. B. T., Booth, R. A., Kirk, J., et al. 2024, MNRAS, 535, 171
Poppenhaeger, K., Ketzer, L., & Mallonn, M. 2021, MNRAS, 500, 4560
Press, W. H., Teukolsky, S. A., Vetterling, W. T., & Flannery, B. P. 1992, Numerical Recipes in C. The Art of Scientific Computing (Cambridge Univ. Press)
Richards, P. G., Fennelly, J. A., & Torr, D. G. 1994, JGR, 99, 8981
Rogers, J. G., Gupta, A., Owen, J. E., & Schlichting, H. E. 2021, MNRAS, 508, 5886
Rogers, J. G., Owen, J. E., & Schlichting, H. E. 2024, MNRAS, 529, 2716
Salz, M., Banerjee, R., Mignone, A., et al. 2015, A&A, 576, A21
Salz, M., Czesla, S., Schneider, P. C., & Schmitt, J. H. M. M. 2016, A&A, 586, A75
Schreyer, E., Owen, J. E., Loyd, R. O. P., & Murray-Clay, R. 2024, MNRAS, 533, 3296
Schulik, M., & Booth, R. A. 2023, MNRAS, 523, 286
Schulik, M., & Owen, J. 2025a, MNRAS, 542, 927
Schulik, M., & Owen, J. E. 2025b, MNRAS, 542, 927
Shull, J. M., & van Steenberg, M. E. 1985, ApJ, 298, 268
Spake, J. J., Sing, D. K., Evans, T. M., et al. 2018, Natur, 557, 68
Spinelli, R., Gallo, E., Haardt, F., et al. 2023, AJ, 165, 200
Tang, Y., Fortney, J. J., & Murray-Clay, R. 2024, ApJ, 976, 221
Tang, Y., Fortney, J. J., Nimmo, F., et al. 2025, ApJ, 989, 28
Thorngren, D. P., Fortney, J. J., Murray-Clay, R. A., & Lopez, E. D. 2016, ApJ, 831, 64
Tian, F., Toon, O. B., Pavlov, A. A., & De Sterck, H. 2005, ApJ, 621, 1049
Verner, D. A., & Ferland, G. J. 1996, ApJS, 103, 467
Vidal-Madjar, A., Lecavelier des Etangs, A., Désert, J. M., et al. 2003, Natur, 422, 143
Virtanen, P., Gommers, R., Oliphant, T. E., et al. 2020, Nature Methods, 17, 261
Wiese, W. L., Fuhr, J. R., & Deters, T. M. 1996, Atomic Transition Probabilities of Carbon, Nitrogen, and Oxygen: A Critical Data Compilation (AIP Press)
Yan, D., Seon, K.-i., Guo, J., Chen, G., & Li, L. 2022, ApJ, 936, 177
Yelle, R. V. 2004, Icar, 170, 167
Yoshida, T., Terada, N., Ikoma, M., & Kuramoto, K. 2022, ApJ, 934, 137
Yoshida, T., Terada, N., & Kuramoto, K. 2024, PEPS, 11, 59
Zhang, M., Knutson, H. A., Dai, F., et al. 2023, AJ, 165, 62